Surface curvature and basal hydraulic stress induce spatial bias in cell extrusion

Authors: Cheng-Kuang Huang[1]*†, Xianbin Yong[2,3]†, David T. She[3,4], Chwee Teck Lim[1,2,3,4]*

Affiliations:

[1]Mechanobiology Institute, National University of Singapore.

[2]Integrative Sciences and Engineering Programme, NUS Graduate School, National University of Singapore.

[3]Department of Biomedical Engineering, National University of Singapore.

[4]Institute for Health Innovation and Technology (iHealthtech), National University of Singapore.

*Corresponding author. Email: mbihc@nus.edu.sg (C.-K. H.); ctlim@nus.edu.sg (C. T. L.).

†These authors contributed equally to this work.

Abstract:

Epithelial cell extrusion is employed in maintaining a healthy epithelium. It remains unclear how environmental conditions specific to various epithelial tissues, such as geometry and fluid osmolarity, affect cell extrusions. We found that, over curved surfaces, epithelial monolayers exhibited higher extrusion rates in concave regions than convex ones. This difference, and overall extrusions, decreased when osmotically induced basal hydraulic stress was reduced by increasing media osmolarity or by culturing monolayers on hydrogels. Mechanistically, basal fluid accumulation antagonized cell-substrate adhesions and the subsequent FAK-Akt survival pathway, leading to apoptotic cell death. Convex surfaces induced cellular forces that acted against osmosis, thereby promoting adhesions and lowering apoptosis. This effect was reversed in concave regions, and together, resulted in the curvature induced spatial bias in cell extrusions.

One-Sentence Summary:

Curvature induces forces in cell-sheets that act against/with osmosis to reduce/elevate fluid stress driven cell extrusions.

Main Text:

Cell extrusion is a coordinated biological process by which epithelial cells are removed from the epithelium without compromising the tissue's natural barrier function *(1-3)*. Typically, in response to external stress, an extrusion disposed cell triggers actomyosin contractions in its neighbors through sphingosine-1-phosphate receptors. The coordinated contraction from its neighbors then squeezes the stressed cell out apically, and concurrently seals the epithelium *(1)*. *In vivo*, the stressors that lead to extrusion events include injuries or mutations *(4, 5)*, crowding *(6),* and morphogenetic cues *(1)*. An often-overlooked fact, however, is that these cell extrusions occur against unique environmental circumstances, such as the characteristic geometries and physical properties of the underlying tissues, and the osmolarity fluctuations in the fluid surrounding them *(2, 7)*. And it is unclear whether some of these environmental cues can contribute to where and when cell extrusions occur, and how. Interestingly, recent findings have shown that in homeostatic tissue, cell extrusions are by no means spatially random *(8)*, as would be expected of a null environmental contribution. Building on the grounds that the biological functions of tissues and organs are often linked to geometric complexities *(9)*, as is the case with the eye or an intestinal villus, in this study, we explored whether surface curvature, the defining property of geometric complexity *(10)*, can also influence epithelial cell extrusions. Supporting this, curved substrates have been extensively shown to affect morphology *(10-13)*, alignment *(14-17)*, migration *(18-20)*, differentiation *(19-21)* and proliferation *(22)* in single adherent cells.

Surface curvature spatially biases epithelial cell extrusions

To explore the effects of surface curvature on epithelial extrusions, repeating wave arrays of hemi-cylindrical valleys and hills with half-period dimensions of c. 200, c. 100, and c. 50 µm (Fig. 1 A to C) were fabricated using a novel microfabrication procedure (see materials and methods, fig. S1 to S3, and table S1). Madin-Darby Canine Kidney (MDCK) type II cells were grown to confluency on these substrates for 24 hours, and then live-cell imaged in a biostation. Figure 1 D to F show representative phase contrast images of confluent MDCK monolayers on these waves. The average cell densities prior to imaging, estimated from nuclei staining (fig. S4), were 2467 ± 282, 2563 ± 245 and 2509 ± 165 cells/mm^2 (M ± SD, n = 19, 25, and 19) for 200, 100, and 50 µm waves, respectively.

Qualitative observations of the monolayers over 24 hours revealed more extruded cells in the concave regions (valleys) than convex ones (hills), on the 100 and 50 µm waves (movies S1 to S3). To properly quantify this valley-hill extrusion difference, an attention-gated residual U-Net was subsequently trained to differentiate actual extrusion events (false cyan highlights in Fig. 1 G and movie S4) from floating debris (confusion matrix in fig. S5 C). The normalized extrusion rate was calculated as the number of extrusions per unit area per 24 hours divided by the initial number of cells per unit area (extrusions×cells^{-1}×24 hours^{-1}).

As shown in figure 1 H (and table S2), a significantly higher mean normalized extrusion rate was found in the valleys compared to hills for monolayers on both the 50 and the 100 µm waves (50 µm valley: 0.325 ± 0.082, 50 µm hill: 0.187 22 ± 0.067; 100 µm valley: 0.308 ± 0.094, 100 µm hill: 0.206 ± 0.071; M ± SD). The valley-hill extrusion rate difference was also higher in the more curved 50 µm wave than the 100 µm wave (0.138 vs 0.103). Meanwhile, no valley-hill extrusion rate difference was found for the 200 µm waves (200 µm valley: 26 0.195 ± 0.099, 200 µm hill: 0.213 ± 0.111; M ± SD). These results suggest that epithelial cell extrusions over curved landscapes depended on both the type (concave or convex), and the degree, of underlying surface curvatures.

To test whether elevated valley extrusions were due to potentially less efficient nutrient and mass transfer in those regions, MDCK monolayers were also cultured on rectangular waves of similar dimensions (fig. S3 D to F, table S1, and movies S5 to S7). As rectangular corners are essentially highly curved surfaces, extrusion sampling regions were defined to exclude these regions. The cell extrusion rate results shown in figure 1 H (and table S2) revealed no differences between valleys and hills on the 200 and 50 μm rectangular waves, while a small valley-hill extrusion rate difference ($\Delta = +0.069$) was seen on the 100 μm rectangular waves. The lack of similarity between cylindrical and rectangular wave extrusion patterns supports that the valley-hill extrusion rate differences seen in the former were curvature induced.

Epithelial cell extrusions can either be apoptotic, or they can be live in response to extreme crowding *(6)*. To test whether the curvature induced extrusion differences were due to surface curvature influencing the relative occurrences of the two extrusion types, we subsequently tracked cell apoptosis. Imaging with the activated caspase 3/7 reporter substrate, CellEvent™, showed that almost all extrusion events, irrespective of location, were accompanied by fluorescence (Fig. 1 I and movie S8). This indicated that the extrusions were apoptotic, and thus valley-hill extrusion rate differences on the waves were not a result of curvature promoting one extrusion type over the other.

Osmotically induced basal hydraulic stress is linked to epithelial cell extrusions

Besides valley-hill differential extrusion rates, live-cell imaging beyond 48 hours (Fig. 2 A and movie S9) typically revealed preferential appearances of fluid-filled domes in the wave valleys. As confluent epithelial monolayers function like semipermeable membranes *(23)*—with cellular tight-junctions permitting the passage of water and preventing it for solutes—this separation of the cell monolayer from the substrate indicated an increasing basal hydraulic stress due to osmotic effects. Specifically, over time, water will tend to move into the basolateral compartments with rising sodium concentrations there due to active ion pumping by basolaterally localized Na+, K+-ATPase *(24)*.

We thus asked if basal hydraulic stress could also underly the extrusion differences observed at earlier time points. To test this, and eliminate any non-specific effects from the solutes, we subjected MDCK monolayers grown on 100 μm waves to 3 independent hyper-osmotic conditions—normal media containing either 4.1 wt. % sucrose, 1 % DMSO, or 0.4 wt. % NaCl (movies S10 to S12). For comparison, a hypo-osmotic condition prepared by diluting normal media with extra 25 % water was also included (movies S13). The measured osmolarities for each condition were 279.3 ± 3.8, 403.6 ± 3.8, 418.6 ± 3.5, 406.3 ± 1.5 and 214.6 ± 4.0 mOsm/L (M ± SD, n = 3) for control, sucrose, DMSO, NaCl and water treatments, respectively.

Strikingly, as shown in figure 2 B (and table S3), by just increasing the osmolarity of the culture media, we were able to significantly reduce the overall cell extrusion rates compared to the control (Control flat: 0.273 ± 0.066, Sucrose flat: 0.115 ± 0.065, DMSO flat: 0.162 ± 0.048, NaCl flat: 0.162 ± 0.048). In addition, the hyper-osmotic treatments were able to reduce the curvature induced valley-hill extrusion rate differences. Specifically, no difference in extrusion rates between the curvature types (flat, valley, and hill) were detected for all three hyper-osmotic treatments. This also suggests that increasing osmolarities affected valley monolayers more.

Consistent with the effects of hyper-osmolarity, diluting media with extra 25 % water to reduce osmolarity resulted in an increase in overall extrusion rates (Control flat: 0.273 ± 0.066, Water flat: 0.457 ± 0.065). Interestingly, valley extrusions did not scale accordingly to maintain a similar valley-hill difference and led to an apparent reversal of the valley-hill extrusion difference

(Water valley: 0.389 ± 0.064, Water hill: 0.470 ± 0.093). This suggests that reduced osmolarities affected hill monolayers more.

Comparison treatments performed by diluting media with 25 % PBS (275.3 ± 0.7 mOsm/L) showed that these elevated extrusions were not due to the associated reduction in nutrients. To further demonstrate that reducing osmolarity by ~65 mOsm/L does not directly kill the cells, and that the elevated extrusions were contingent upon a full monolayer (i.e., a semi-permeable membrane), we imaged sub-confluent MDCK monolayers subjected to the same hypo-osmotic treatment (movie S14); the cells proliferated normally with negligible cell deaths.

As cell adhesions give way to hydraulic stress, the accumulation of fluid is inevitable. To verify the existence of such nascent fluid spaces beneath MDCK monolayers, reflection interference contrast microscopy (RICM) was employed. Relying on the interference of reflected light from the substrate and the cell membrane, the method produces image intensities that are sensitively coupled to basal membrane distances from the substrate *(25-27)*. In particular, it has been verified that attached cellular regions (e.g., focal adhesions) appear the darkest, with intensities increasing with basal separation *(25, 26)*. Our RICM time-lapse observations (Fig. 2 C and movie S15) indeed revealed numerous continuously moving bright regions (i.e., fluid spaces) under MDCK monolayers on planar substrates. Interestingly, optical flow analysis *(28)* performed on the sequences showed a qualitative correspondence between the directions of the fluid motion (flow paths in Fig. 2 C) and focal adhesion disassembly (dark streaks fading).

To show that changing osmolarity was sufficient in tuning these basal separations, we tracked variations in the RICM intensities of monolayers grown on planar surfaces and pre-conditioned in hyper-osmotic 4.1 wt. % sucrose media, followed by the addition of water to reinstate iso-osmolarity (Fig. 2 D and movie S16). As osmolarity was lowered back to normal, fluid-filled spaces (asterisks in Fig. 2 D) begin to develop and eventually span underneath several cells. Moreover, unlike domes, these nascent basal fluid spaces cannot be inferred from the bright-field images. The minimum grey value aligned histograms of each timeframe plotted against time (Fig. 2 E) showed the central tendencies of the image histograms shifting toward higher intensities upon the addition of water. This indicated that the basal cell membranes were moving further away from the substrate. Furthermore, the averaged median grey values of the treatment segments (Fig. 2 F) showed a ~9 % intensity increase from hyper- to iso-osmotic treatment segments. This finding strengthens the link between osmotically induced basal hydraulic stress and the osmolarity dependent extrusion rates.

We subsequently examined whether similar basal separation differences exist between valley and hill monolayers on the curved waves. Minimum-grey-value aligned RICM max-projections of MDCK monolayers on the various curvature types of 100 μm waves (Fig. 2 G), showed image contrasts that appeared darkest on the hills and brightest in the valleys. As shown in figure 2 H, image median grey values of valleys were ~60 % higher than those of the hills. These results suggest that hill monolayers were more closely apposed to the surface as compared to their valley counterparts and parallels the basal separation differences observed in hyper- and iso-osmotic treatments.

To further rule out any cryptic effects of changing osmolarity, we tracked MDCK monolayers cultured on hydrogel substrates in iso-osmotic medium. Being water and solute permeable materials, hydrogels can buffer against drastic increase in solute concentrations, thereby lowering osmosis induced hydraulic stress. And to eliminate the possibility that any extrusion differences were due to hydrogels being a much softer material (~30 kPa *(22)*), MDCK

monolayers cultured on silicone substrates of similar stiffness (~25 kPa *(29)*) were also tracked (Fig. 3 A and movie S17). Figure 3 B (and table S5) shows that the extrusion rate differences between the materials were significant. Compared to monolayers on stiff silicone substrates, monolayers on polyacrylamide (PAM) gels produced fewer extrusions over 24 hours ($\Delta = -0.168$). Furthermore, monolayers on soft silicone substrates exhibited higher extrusion rates than their counterparts on stiff silicones ($\Delta = +0.096$). Notably, monolayers on PAM hydrogels typically reached higher cell densities, due to the fewer extrusions and therefore more dividing cells.

Surface curvature induced cell-sheet force asymmetry modulates osmotic effects

While reduced basal separation in hyper-osmotic treatments can be achieved through drawing water from the basal side by osmosis, it is unlikely that neighboring valley and hill regions are subjected to differing osmolarities in the same medium. Instead, judging from geometry, if out-of-plane epithelial forces consistently pointed into the substrates in the hill regions, they would effectively work against osmosis induced basal hydraulic stress and promote adhesion formation and persistence. This will sufficiently account for the smaller basal-to-substrate separation. In support of this, nuclei were readily observed deformed against the surface on the hills (Fig. 3 C). We subsequently determined the epithelial force distributions over our wave substrates using a finite element-based 3D force microscopy (see materials and methods and fig. S6). Figure 3 D shows a representative monolayer normal-force distribution on a 100 µm wave, unwrapped and flattened as a 2D projection (see materials and methods for unwrapping algorithm). On these waves, the magnitudes of the forces varied consistently over the period, with monolayers on the hills producing larger forces. Interestingly, this effect appeared to be curvature dependent (Fig. 3 E), with 50 µm waves showing the greatest range of magnitudes while the 200 µm structures having an approximately even distribution of force magnitudes along the curved landscape (50 µm: [1.138, 10.972]; 100 µm: [1.116, 7.725]; and 200 µm: [1.955, 4.356] $nN/\mu m^2$). And as was predicted from nuclei deformation, the directions of the normal forces (Fig. 3 F) were in general pointing into the substrate on the hills for both the 50 and 100 µm waves. This normal force component decreased as we move away from the hills, flipping to an outward pointing direction at the valley-hill interface. The 200 µm waves did not exhibit any clear curvature dependent force direction patterns, and is in accordance with the lack of valley-hill extrusion difference seen earlier. Taken together, this curvature induced force symmetry breaking provided the means for establishing differential basal separation between valley and hill cell monolayers.

Basal hydraulic stress antagonizes FAK tyr397 autophosphorylation and its downstream survival signaling

As cell adhesions are intimately related to cell survival *(30)*, we hypothesized that basal hydraulic stress may be inducing the apoptotic cell extrusions by antagonizing cell-substrate adhesions. A likely mechanism is through the reduction of focal adhesion kinase (FAK) auto-phosphorylation at tyrosine residue 397 (tyr397), which will ultimately downregulate the downstream Akt survival cascade *(31)*. From this, we predicted that the pro-survival effects of hyper-osmolarity would be abolished if FAK inhibitors were introduced together. We tested this by introducing 3 µM of FAKI14 (specific FAK inhibitor at tyr397) to hyper-osmotic 4.1 wt. % sucrose media—sucrose being the most inert of the 3 hyper-osmotic treatments to cells—and imaged for 24 hours (movie S18).

As predicted, our results (Fig. 4 A and table S6) revealed higher extrusion rates when FAKI14 inhibitor was added with sucrose, as compared to the sucrose treatment alone (e.g., FAKI14 flat: 0.280 ± 0.073 vs Sucrose flat: 0.115 ± 0.065), in all three curvature types. In addition,

the extrusion rates in FAKI14 treated samples were similar to that in the control for both the flat and valley regions. While the hill region differences in these two conditions were statistically significant, the difference was smaller than the hill region differences between control and sucrose alone. The valley-hill extrusion rate difference was also restored in the FAKI14 treatment (Δ = +0.183) despite higher media osmolarity. Further increasing the FAKI14 concentrations to 6 μM (Fig. 4 B and movie S19) induced massive cell deaths and led to monolayer disintegration.

To show that modulation of osmolarity affected Akt signaling in a FAK dependent manner, we immunoblotted and quantified the protein expression levels of MDCK monolayers cultured in hyper-osmotic, hypo-osmotic, and iso-osmotic media, and, for comparison, also on soft silicones and PAM hydrogels (Fig. 4 C to E). Significantly higher levels of phosphorylated-FAK (p-FAK) and phosphorylated-Akt (p-Akt) were observed in media supplemented with sucrose (hyper-osmotic) as compared to those in the iso-osmotic control group. These findings agree with previous reports of higher activated Akt levels in epithelial cells subjected to hyper-osmotic treatment *(32)*. Interestingly, FAK activation in the hypo-osmotic condition was not significantly different to the control; this reflects the fact that dead extruded cells cannot be sampled through immunoblotting. Similarly, although the level of p-Akt was reduced under hypo-osmotic treatment, it did not include responses from already extruded cells. On the other hand, cells cultured on PAM hydrogels revealed significantly elevated levels of both p-FAK and p-Akt compared to those on stiff and soft silicones, and the extent of Akt activation was even more prominent (2.5-fold increment) than cells in hyper-osmotic media. Collectively, our findings indicated that monolayers maintained in reduced basal hydraulic stress (hyper-osmotic media and hydrogels) exhibited higher levels of FAK and Akt activation. All else being equal, this will lead to an up-regulation of survival signals that ultimately translates to lower apoptotic cell extrusions.

To show that the same mechanism underlies the valley-hill cell extrusion rate differences over our curved substrates, we visualized p-FAK and FAK on 100 μm waves (Fig. 4 F). Prior normalizations were applied to the images (see materials and methods) to compare the relative activation of p-FAK/FAK between hill and valley monolayers (Fig. 4 G and table S8). In accordance with our observed higher valley extrusion rates, valley cells exhibited ~20 % lower p-FAK/FAK intensity ratios as compared to hill cells. This predisposes the cells in the valley to a higher likelihood of being extruded as compared to the cells on the hills, resulting in the apparent curvature dependent extrusion rate differences.

Discussions

Our investigations demonstrate that when cultured on hemi-cylindrical wave substrates, an emergent spatial bias in cell extrusions was elicited in confluent epithelial monolayers. Specifically, MDCK monolayers in valley (concave) regions exhibited significantly higher cell extrusion rates than their counterparts in hill (convex) regions. And this difference was both dependent on the sense (positive or negative) and the degree of curvature.

Increasing media osmolarity sufficiently reduced this spatial bias, and overall cell extrusion numbers whereas reducing osmolarity increased overall cell extrusions. Imaging planar monolayer basal regions revealed extensive dynamic fluid spaces that responded to osmolarity changes, with lower osmolarity resulting in larger basal fluid spaces, and vice versa. As epithelial monolayers functions like semi-permeable membranes, inhibiting solute transport but permitting water, these observations forge a link between the cell-substrate separation induced by osmotically driven basal hydraulic stress and epithelial cell extrusions. On the other hand, on curved substrates without

osmolarity perturbations, basal fluid spaces under monolayers in hill regions were found consistently smaller than those in valley regions. With typical extrusion rates higher in the valleys, again, a similar link is established between basal separation and cell extrusions. We subsequently found that curvature induced cellular force symmetry-breaking results in hill region out-of-plane forces pushing cells down on the surface, against osmotically induced basal hydraulic stress and cell-substrate separation whereas a reversed effect was seen in the valleys. Moreover, the force patterns are in accordance with the curvature induced valley-hill extrusion differences. Specifically, larger valley-hill force differences correlated with larger valley-hill extrusion differences, with 200 μm waves showing no effect in both phenomena. It is worth noting that cellular forces on the hills cannot indefinitely protect cells against osmotically induced fluid stress and should depend on the strength of apical-basal osmotic gradient. This is evidenced by the fact that hypo-osmotic treatments affected hill monolayers more than valley ones, demonstrating that, given sufficient osmotic potential, basal fluid stress can overcome the inward collective cellular forces.

Basal hydraulic stress' role in epithelial cell extrusions is further supported by the reduced extrusion rates seen, independent of osmolarity perturbations, in monolayers cultured on hydrogel substrates. These type of substrates permits both solute and water and can therefore reduce hikes in solute concentration due to apical-to-basal ion displacement by the cells. Interestingly, monolayers on the hydrogel substrates typically reach higher cell densities. We attribute this to the fewer extruded cells and therefore more dividing cells. This also indicates that the cell extrusions seen in our study are not of the crowding induced kind.

As basal fluid motion frequently displaced focal adhesions, we hypothesized that the reduced focal adhesion signaling contributed to the cell extrusions observed. Indeed, incorporating focal adhesion kinase inhibitors in high osmolarity treatments re-elevated cell extrusions, indicating the latter's pro-survival effects were related to cell adhesion formation. Further supporting our hypothesis, immunoblotting analysis revealed higher activation of both focal adhesion kinase and the downstream survival hub protein Akt, in conditions with reduced basal hydraulic stress; that is, monolayers in hyper-osmotic media or on hydrogel substrates. Likewise, on the waves, paralleling the basal separations seen from RICM, higher FAK activation was also observed in monolayers in hill regions compared to their counterparts in valley regions. All else being equal, this will lead to a downregulation of survival signals in valley monolayers and ultimately establishing the apparent spatial bias in extrusion rate differences.

Recent developments have shown that curved surfaces can direct intestinal epithelial cell differentiation through shaping morphogen gradients *(33)* and also influence intracellular YAP/TAZ localization *(34)*. Moreover, lumenal hydraulic stress has been shown to drive cell patterning in blastocyst development *(35)*. Our findings now reveal that surface curvature and hydraulic stress spatially biases epithelial cell extrusions. Remarkably, basal hydraulic stress alone was sufficient in inducing epithelial cell extrusion; specifically, by disrupting cell adhesions and inhibiting downstream Akt survival signals (Fig. 4 H and I). And an emergent spatial pattern in cell extrusions was elicited when fluid stress was coupled with curvature induced symmetry breaking of collective cellular forces. Specifically, positive surface curvatures induced inward out-of-plane forces that acted against basal hydraulic stress, favoring cell-substrate adhesion and survival. Meanwhile, a reversal of this effect occurred on negatively curved surfaces (Fig. 4 J). Through our investigation, we have shown that curved surfaces can, similar to single cells, also elicit differential responses in multicellular structures. Furthermore, our study has significant *in vivo* implications in that such selective removal of cells can easily lead to segregated populations

of differentiated cells and could well be employed during morphogenesis. Moreover, the net effect of collective cellular forces on the positive hills likens reverse osmosis. It is thus of fundamental interest to explore in future whether such collective cellular forces are utilized in a similar way in the body to regulate water transport and solute concentrations in homeostasis and/or direct development.

References and Notes

1. S. Ohsawa, J. Vaughen, T. Igaki, Cell extrusion: a stress-responsive force for good or evil in epithelial homeostasis. *Developmental Cell* **44**, 284–296 (2018). Doi: 10.1016/j.devcel.2018.01.009
2. L. W. Peterson, D. Artis, Intestinal epithelial cells: regulators of barrier function and immune homeostasis. *Nature Reviews Immunology* **14**, 141–153 (2014). Doi: 10.1038/nri3608
3. G. Slattum, K. M. McGee, J. Rosenblatt, P115 RhoGEF and microtubules decide the direction apoptotic cells extrude from an epithelium. *Journal of Cell Biology* **186**, 693–702 (2009). Doi: 10.1083/jcb.200903079
4. T. Chiba, E. Ishihara, N. Miyamura, R. Narumi, M. Kajita, Y. Fujita, A. Suzuki, Y. Ogawa, H. Nishina, MDCK cells expressing constitutively active Yes-associated protein (YAP) undergo apical extrusion depending on neighboring cell status. *Scientific Reports* **6**,1–10 (2016). Doi: 10.1038/srep28383
5. Y. Gu, J. Shea, G. Slattum, M. A. Firpo, M. Alexander, S. J. Mulvihill, V. M. Golubovskaya, J. Rosenblatt, Defective apical extrusion signaling contributes to aggressive tumor hallmarks. *eLife* **4**, e04069 (2015). Doi: 10.7554/eLife.04069
6. G. T. Eisenhoffer, P. D. Loftus, M. Yoshigi, H. Otsuna, C. B. Chien, P. A. Morcos, J. Rosenblatt, Crowding induces live cell extrusion to maintain homeostatic cell numbers in epithelia. *Nature* **484**, 546–549 (2012). Doi: 10.1038/nature10999
7. L. G. Van Der Flier, H. Clevers, Stem cells, self-renewal, and differentiation in the intestinal epithelium. *Annual Review of Physiology* **71**, 241–260 (2009). Doi: 10.1146/annurev.physiol.010908.163145
8. D. Krndija, F. El Marjou, B. Guirao, S. Richon, O. Leroy, Y. Bellaiche, E. Hannezo, D. M. Vignjevic, Active cell migration is critical for steady-state epithelial turnover in the gut. *Science* **365**, 705–710 (2019). Doi: 10.1126/science.aau3429
9. D. W. Thompson, *On growth and form* (Cambridge Univ. Press, Cambridge, 1942).
10. S. J. P. Callens, R. J. C. Uyttendaele, L. E. Fratila-Apachitei, A. A. Zadpoor, Substrate curvature as a cue to guide spatiotemporal cell and tissue organization. *Biomaterials* **232**, 119739 (2020). Doi: 10.1016/j.biomaterials.2019.119739
11. D. Baptista, L. Teixeira, C. van Blitterswijk, S. Giselbrecht, R. Truckenmüller, Overlooked? underestimated? effects of substrate curvature on cell behavior. *Trends in Biotechnology* **37**, 838–854 (2019). Doi: 10.1016/j.tibtech.2019.01.006
12. J.-Y. Lin, W.-J. Lin, W.-H. Hong, W.-C. Hung, S. H. Nowotarski, S. M. Gouveia, I. Cristo, K.-H. Lin, Morphology and organization of tissue cells in 3D microenvironment of monodisperse foam scaffolds. *Soft Matter* **7**, 10010, (2011). Doi: 10.1039/C1SM05371J

13. Y. A. Rovensky, V. I. Samoilov, Morphogenetic response of cultured normal and transformed fibroblasts, and epitheliocytes, to a cylindrical substratum 16 surface: Possible role for the actin filament bundle pattern. *Journal of Cell Science* **107**, 1255–1263 (1994). Doi: 0.1242/jcs.107.5.1255

14. P. Weiss, Experiments on cell and axon orientation in vitro: The role of colloidal exudates in tissue organization. *Journal of Experimental Zoology* **100**, 353–386 (1945). Doi: 10.1002/jez.1401000305

15. C. M. Hwang, Y. Park, J. Y. Park, K. Lee, K. Sun, A. Khademhosseini, S. H. Lee, Controlled cellular orientation on PLGA microfibers with defined diameters. *Biomedical Microdevices* **11**, 739–746 (2009). Doi: 10.1007/s10544-009-9287-7

16. S. M. Yu, B. Li, F. Amblard, S. Granick, Y. K. Cho, Adaptive architecture and mechanoresponse of epithelial cells on a torus. *Biomaterials* **265,** 120420 **(**2021). Doi: 10.1016/j.biomaterials.2020.120420

17. V. Hosseini, P. Kollmannsberger, S. Ahadian, S. Ostrovidov, H. Kaji, V. Vogel, A. Khademhosseini, Fiber-Assisted Molding (FAM) of surfaces with tunable curvature to guide cell alignment and complex tissue architecture. *Small* **10**, 4851–4857 (2014). Doi: 10.1002/smll.201400263

18. K. H. Song, S. J. Park, D. S. Kim, J. Doh, Sinusoidal wavy surfaces for curvature-guided migration of Tlymphocytes. *Biomaterials* **51**, 151–160 (2015). Doi: 10.1016/j.biomaterials.2015.01.071

19. L. Pieuchot, J. Marteau, A. Guignandon, T. Dos Santos, I. Brigaud, P. Chauvy, T. Cloatre, A. Ponche, T. Petithory, P. Rougerie, M. Vassaux, J. Milan, N. T. Wakhloo, A. Spangenberg, M. Bigerelle, K. Anselme, Curvotaxis directs cell migration through cell-scale curvature landscapes. *Nature Communications* **9**, 3995 (2018). Doi: 10.1038/s41467-018-06494-6

20. T. Yamashita, P. Kollmannsberger, K. Mawatari, T. Kitamori, V. Vogel, Cell sheet mechanics: How geometrical constraints induce the detachment of cell sheets from concave surfaces. *Acta Biomaterialia* **45**, 85–97 (2016). Doi: 10.1016/j.actbio.2016.08.044

21. M. Werner, S. B.G. Blanquer, S. P. Haimi, G. Korus, J. W. C. Dunlop, G. N. Duda, D. W. Grijpma, A. Petersen, Surface curvature differentially regulates stem cell migration and differentiation via altered attachment morphology and nuclear deformation. *Advanced Science* **4**, 1–11 (2017). Doi: 10.1002/advs.201600347

22. C.-K. Huang, G. J. Paylaga, S. Bupphathong, K.-H. Lin, Spherical microwell arrays for studying single cells and microtissues in 3D confinement. *Biofabrication* **12**, 025016 (2020). Doi: 10.1088/1758-5090/ab6eda

23. K. R. Spring, Epithelial fluid transport—a century of investigation. *Physiology*, **14**, 92–98 (1999). Doi: 10.1152/physiologyonline.1999.14.3.92

24. N. A. Abaza, J. Leighton, S. G. Schultz, Effects of ouabain on the function and structure of a cell line (MDCK) derived from canine kidney: I. light microscopic observations of monolayer growth. *In Vitro: Journal of the Tissue Culture Association*, **10**,172–183 (1974). Doi: 10.1007/BF02615230

25. A. S. G. Curtis, The mechanism of adhesion of cells to glass: a study by interference reflection microscopy. *Journal of Cell Biology* **20**, 199–215 (1964). Doi: 10.1083/jcb.20.2.199

26. J. P. Heath, G. A. Dunn, Cell to substratum contacts of chick fibroblasts and their relation to the microfilament system. A correlated interference-reflexion and high-voltage electron-microscope study. *Journal of Cell Science* **29**, 197–212 (1978). Doi: 10.1242/jcs.29.1.197

27. L. Limozin, K. Sengupta, Quantitative reflection interference contrast microscopy (RICM) in soft matter and cell adhesion. *ChemPhysChem* **10**, 2752–2768 (2009). Doi: 10.1002/cphc.200900601

28. X. Yong, C.-K. Huang, C. T. Lim, An integrated platform to facilitate the calculation, validation and visualization of optical flow velocities in biological images. *Journal of The Royal Society Interface*, **18**, 20210248 (2022). Doi: 10.1098/rsif.2021.0248

29. K. M. C. Leong, M. H. Nai, F. C. Cheong, C. T. Lim. Viscoelastic effects of silicone gels at the micro- and nanoscale. *Procedia IUTAM* **12**, 20–30 (2015). Doi: 10.1016/j.piutam.2014.12.004

30. P. J. Reddig, R. L. Juliano, Clinging to life: cell to matrix adhesion and cell survival. *Cancer and Metastasis Reviews* **24**, 425–439 (2005). Doi: 10.1007/s10555-005-5134-3

31. S. K. Hanks, L. Ryzhova, N.-Y. Shin, J. Brábek, Focal adhesion kinase signaling activities and their implications in the control of cell survival and motility. *Frontiers in Bioscience-Landmark* **8**, 982–996 (2003). Doi: 10.2741/1114

32. Y. Terada, Seiji Inoshita, S. Hanada, H. Shimamura, M. Kuwahara, W. Ogawa, M. Kasuga, S. Sasaki, F. Marumo, Hyperosmolality activates Akt and regulates apoptosis in renal tubular cells. *Kidney International* **60**, 553–567 (2001). Doi: 10.1046/j.1523-1755.2001.060002553.x

33. A. E. Shyer, T. R. Huycke, C. Lee, L. Mahadevan, C. J. Tabin, Bending gradients: how the intestinal stem cell gets its home. *Cell* **161**, 569–580 (2015). Doi: 10.1016/j.cell.2015.03.041

34. M. Luciano, S. L. Xue, W. H. De Vos, L. Redondo-Morata, M. Surin, F. Lafont, E. Hannezo, S. Gabriele, Cell monolayers sense curvature by exploiting active mechanics and nuclear mechanoadaptation. *Nature Physics* **17**, 1382–1390, (2021). Doi: 10.1038/s41567-021-01374-1

35. C. J. Chan, M. Costanzo, T. Ruiz-Herrero, G. Mönke, R. J. Petrie, M. Bergert, A. Diz-Muñoz, L. Mahadevan, T. Hiiragi, Hydraulic control of mammalian embryo size and cell fate. *Nature* **571**, 112– 116 (2019). Doi: 10.1038/s41586 019-1309-x

36. C. Liu, J. Xu, S. He, W. Zhang, H. Li, B. Huo, Ba. Ji, Collective cell polarization and alignment on curved surfaces. *Journal of the Mechanical Behavior of Biomedical Materials* **88**, 330–339 (2018). Doi: 10.1016/j.jmbbm.2018.08.014

37. C.-K. Huang, A. Donald, Revealing the dependence of cell spreading kinetics on its spreading morphology using microcontact printed fibronectin patterns. *Journal of The Royal Society Interface* **12**, 20141064–20141064 (2014). Doi: 10.1098/rsif.2014.1064

38. M. Drozdzal, E. Vorontsov, G. Chartrand, S. Kadoury, C. Pal, "The Importance of Skip Connections in Biomedical Image Segmentation" in *Deep Learning and Data Labeling for Medical Application*, G. Carneiro, D. Mateus, L. Peter, A. Bradley, J. Manuel, R. S. Tavares, V. Belagiannis, J. Paulo Papa, J. C. Nascimento, M. Loog, Z. Lu, J. S. Cardoso, J. Cornebise, Eds. (Springer, Cham, 2016), pp. 179-187. Doi: doi.org/10.1007/978-3-319-46976-8

39. T. He, Z. Zhang, H. Zhang, Z. Zhang, J. Xie, M. Li, "Bag of Tricks for Image Classification with Convolutional Neural Networks" in *2019 IEEE/CVF Conference on Computer Vision and*

Pattern Recognition (CVPR), pp. 558–567, Long Beach, CA, June 2019. IEEE. Doi: 10.1109/CVPR41558.2019

40. K. He, X. Zhang, S. Ren, J. Sun, "Identity Mappings in Deep Residual Networks" in *Computer Vision – ECCV 2016*, B. Leibe, J. Matas, N. Sebe, M. Welling, Eds. (Springer, Cham, 2016) vol. 9908, pp. 630–645. Doi: doi.org/10.1007/978-3-319-46448-0

41. J. Hu, L. Shen, G. Sun. "Squeeze-and-Excitation Networks" in *2018 IEEE/CVF Conference on Computer Vision and Pattern Recognition*, pp. 7132–7141, Salt Lake City, UT, June 2018. IEEE. Doi: 10.1109/CVPR40276.2018

42. J. Schlemper, O. Oktay, M. Schaap, M. Heinrich, B. Kainz, B. Glocker, D. Rueckert, Attention gated networks: Learning to leverage salient regions in medical images. *Medical Image Analysis* **53**, 197–207 (2019). Doi: 10.1016/j.media.2019.01.012

43. M. Yeung, E. Sala, C.-B. Schönlieb, L. Rundo, Unified focal loss: generalising dice and cross entropy-based losses to handle class imbalanced medical image segmentation. *Computerized Medical Imaging and Graphics* **95**, 102026 (2022). Doi: 10.1016/j.compmedimag.2021.102026

44. Q. Zhu, B. Du, B. Turkbey, P. L. Choyke, P. Yan, "Deeply-Supervised CNN for Prostate Segmentation" in *2017 International Joint Conference on Neural Networks (IJCNN)*, pp. 178–184, Anchorage, AK, May 2017. IEEE. Doi: 10.1109/IJCNN39090.2017

45. M. Islam, B. Glocker, "Spatially Varying Label Smoothing: Capturing Uncertainty from Expert Annotations" in *Information Processing in Medical Imaging*, A. Feragen, S. Sommer, J. Schnabel, M. Nielsen, Eds. (Springer, Cham, 2021) vol. 12729, pp. 677–688. Doi: 10.1007/978-3-030-78191-0

46. I. Bello, W. Fedus, X. Du, E. D. Cubuk, A. Srinivas, T.-Y. Lin, J. Shlens, B. Zoph, Revisiting resnets: Improved training and scaling strategies. *Advances in Neural Information Processing Systems* **34** (2021).

47. U. Schmidt, M. Weigert, C. Broaddus, G. Myers, "Cell Detection with Star-Convex Polygons" in *Medical Image Computing and Computer Assisted Intervention–MICCAI 2018*, A. F. Frangi, J. A. Schnabel, C. Davatzikos, C. Alberola-López, G. Fichtinger, Eds. (Springer, Cham, 2018) vol. 11071, pp. 265–273. Doi: 10.1007/978-3-030-00937-3

48. G. Farnebäck, "Two-Frame Motion Estimation Based on Polynomial Expansion" in *Image Analysis*, G. Goos, J. Hartmanis, J. van Leeuwen, J. Bigun, T. Gustavsson, Eds. (Springer, Berlin, 2003) vol. 2749, pp. 363–370. Doi: 10.1007/3-540-45103-X_50

Acknowledgments:

We would like to thank the National University of Singapore (NUS) Mechanobiology Institute for the support, facilities and resources provided during this work. We would also like to thank Dr. Natalia Veronica and Dr. Wan Sia Heng at the Department of Pharmacy, NUS, for assisting in the measurement of the media osmolality, and our colleague Dr. Chii Jou Chan for his suggestions and advice on the paper. X.Y. is supported by the Integrative Sciences and Engineering Programme Scholarship from the NUS Graduate School.

Funding:

Human Frontier Science Program Research Grant 233 [grant number RGP0038/2018]

Author contributions:

Conceptualization: CKH, XY

Methodology: CKH, XY

Investigation: CKH, XY, DTS

Formal analysis: CKH, XY, DTS

Visualization: CKH, XY, DTS

Funding acquisition: CTL

Project administration: CKH, CTL

Resources: CTL

Software: CKH, XY

Supervision: CTL

Writing – original draft: CKH, XY, DTS

Writing – review & editing: CTL

Competing interests:

We declare that we have no competing interests.

Data and materials availability:

Processed datasets can be obtained from ScholarBank@NUS (https://doi.org/10.25540/XT13-8VRZ). Due to the large size of our raw data, these are available only upon reasonable request. Custom codes and scripts can be found in the following locations. The codes for 3DTFM can be found at https://github.com/yongxb/3DTFM and the companion GPU/CUDA optimized 3D Farneback algorithm can be found at https://github.com/yongxb/OpticalFlow3d. The implementation of the neural network used to detect extrusion events can be found at https://github.com/yongxb/Unet-extrusion-detection. They have also been deposited in ScholarBank@NUS (https://doi.org/10.25540/XT13-8VRZ), along with the R scripts for RICM.

Supplementary Materials

Materials and Methods

Figs. S1 to S6

Tables S1 to S8

References (*36–48*)

Movies S1 to S19

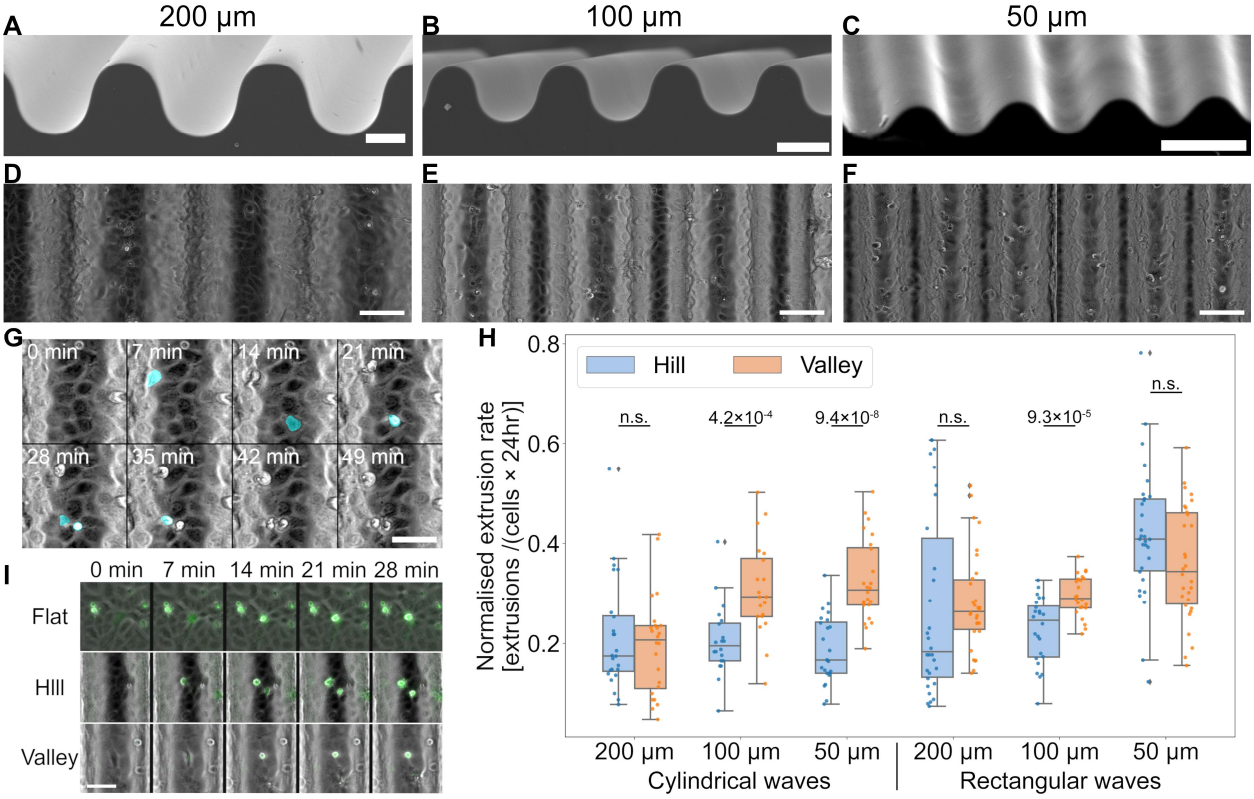

Fig. 1. Epithelial monolayers exhibit higher cell extrusion rates in negatively curved valleys of hemi-cylindrical wave substrates. (**A**-**C**) SEM images of cylindrical wave structures with half-periods 200, 100 and 50 µm. Scale-bar: 100 µm. (**D**-**F**) Phase contrast images of confluent MDCK monolayers on 200, 100 and 50 µm waves, 24 hours after seeding. (**G**) Time-lapse excerpts demonstrating extrusion event registration (cyan objects) using our trained neural network. (**H**) Boxplot of extrusion events registered over 24 hours, on 200, 100 and 50 µm cylindrical waves, and on 200, 100 and 50 µm rectangular waves for comparison. Box shows the interquartile range (IQR) while whiskers are 1.5×IQR. Detailed statistics can be found in table S1. (**I**) Multi-channel time-lapse excerpts of cells incubated with activated caspase 3/7 reporter (false green over phase contrast), on flat, hill and valley regions of a 100 µm wave: fluorescence indicate dying cells. Scale-bars (unless otherwise stated): 50 µm.

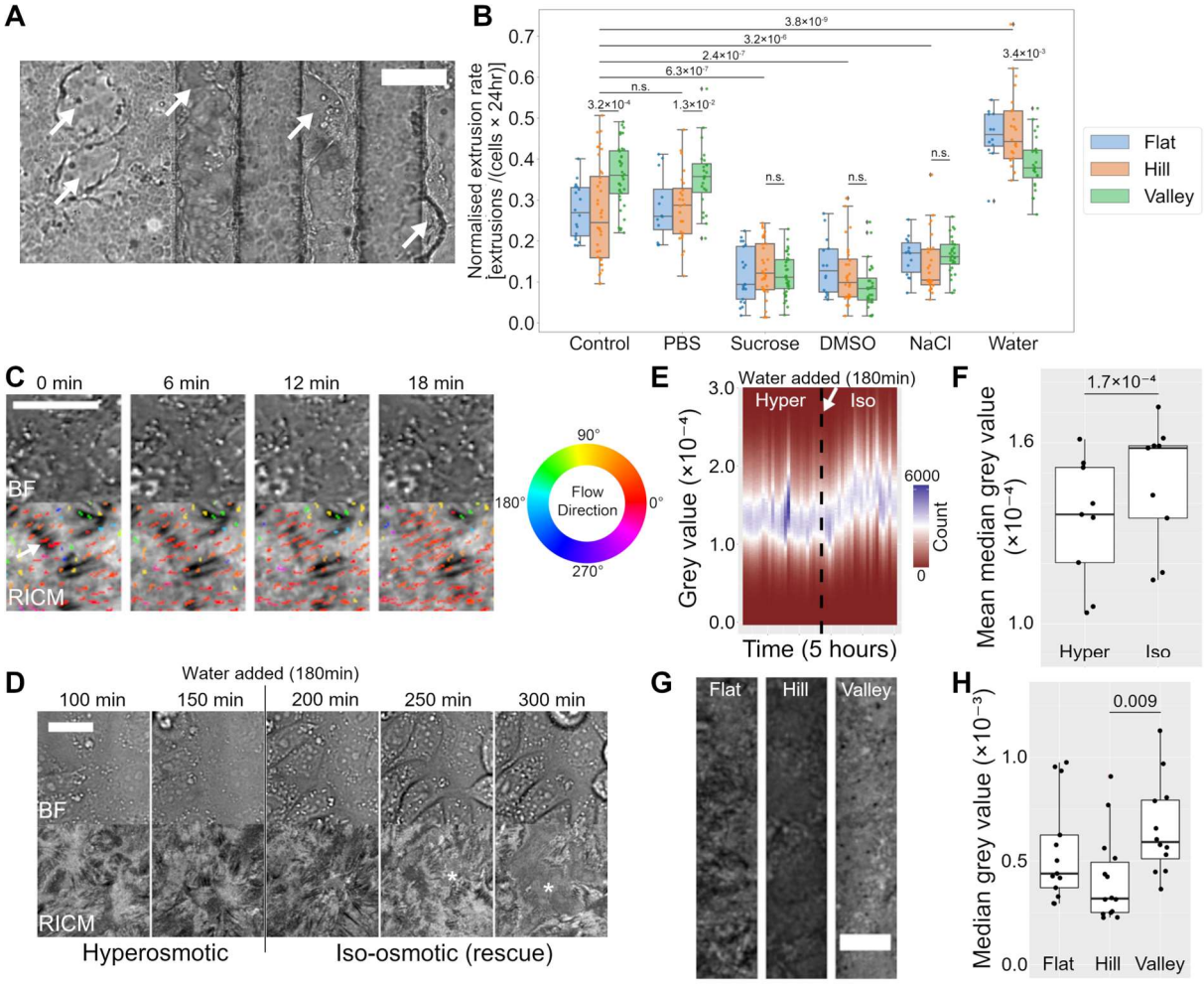

Fig. 2. Osmosis induced basal hydraulic stress is linked to cell extrusions. (**A**) Confluent MDCK II monolayers form fluid-filled domes (arrows) in wave valleys when cultured for over 48 hours. Scale-bar: 100 µm. (**B**) Boxplot of extrusions per cell over 24 hours on 100 µm cylindrical waves, with monolayers subjected to osmolarity perturbations that included the addition of 4.1 wt. % sucrose, 1 % DMSO, 0.4 wt. % NaCl, 25 % water, and 25 % PBS. Box shows the interquartile range (IQR) while whiskers are 1.5×IQR. Detailed statistics can be found in table S3. (**C**) Bright-field/RICM time-lapse excepts showing dynamic basal fluid spaces whose motion (direction encoded colored paths) corresponded with the direction of focal adhesion (dark streaks e.g. indicated by white arrow) disassembly. (**D**) Bright-field/RICM time-lapse excepts showing the accumulation of basal fluid (asterisks) when iso-osmolarity was reinstated (at 180 min) in hyper-osmotically pre-conditioned monolayers. (**E**) Plot of the image histograms against time showing an increase in grey values as iso-osmolarity was restored, indicating a general increase in basal-to-substrate separations with decreasing apical media osmolarity. (**F**) Boxplot of histogram median grey values from (**E**) averaged separately over the duration of hyper- and iso-osmolarity treatments. Detailed statistics can be found in table S4. (**G**) Representative max-projected RICM z-stacks of flat, hill and valley regions. (**H**) Boxplot of histogram median grey values from images such as in (**G**). Detailed statistics can be found in table S4. Scale-bars in (**C**), (**D**), (**G**): 20 µm.

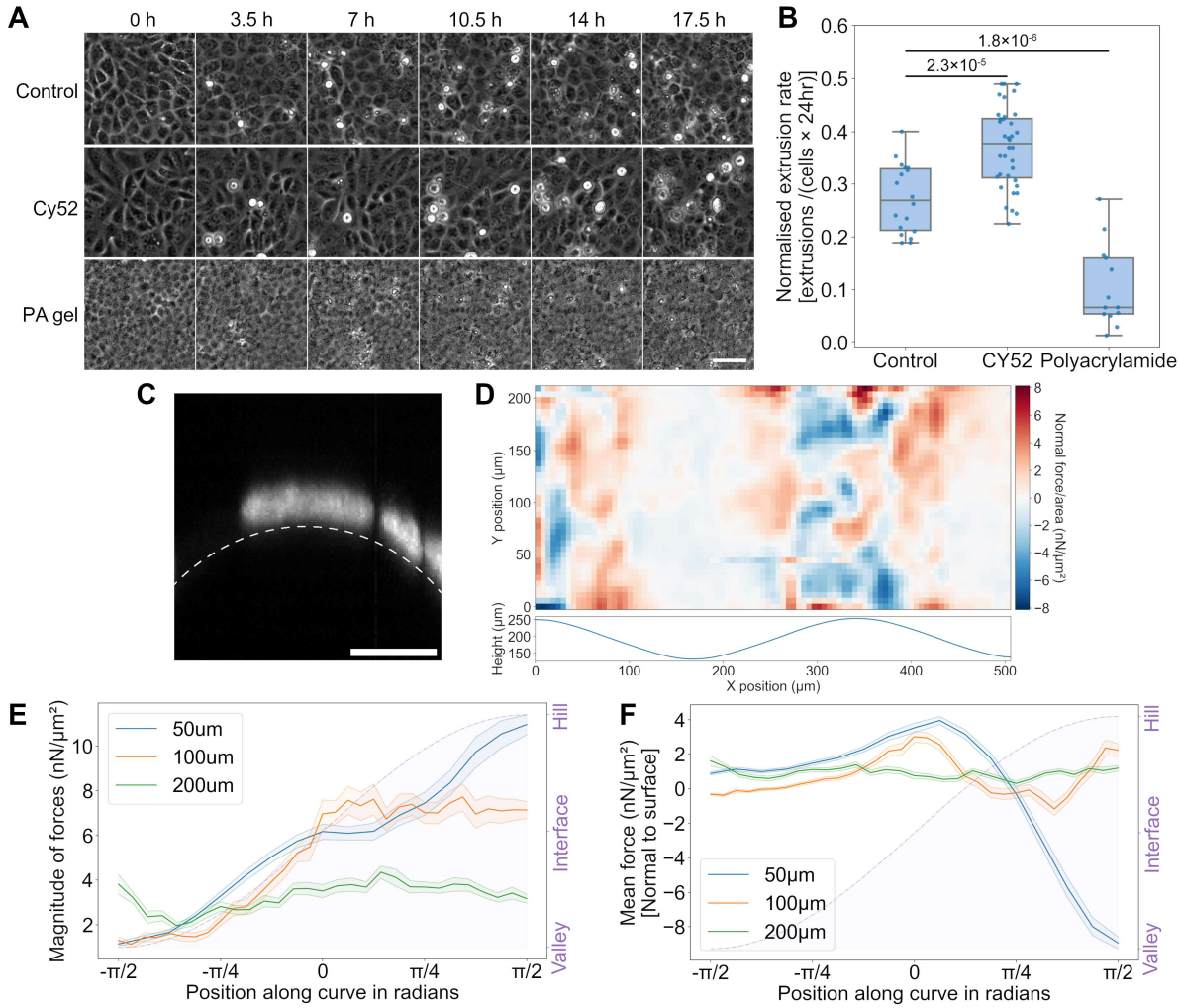

Fig. 3. Solute permeable hydrogel substrates reduce epithelial cell extrusions, and surface curvature induces symmetry breaking in collective cellular forces. (**A**) Time-lapse excerpts showing cell extrusion accumulation on stiff PDMS (control), and on soft silicone and PAM hydrogel of similar stiffness (scale bar: 50 µm). (**B**) Boxplot showing the cell extrusion rates from the 3 substrates in (**A**). Box shows the interquartile range (IQR) while whiskers are 1.5×IQR. Detailed statistics can be found in table S6. (**C**) Nuclei fluorescence cross-section shows deformation against surface on wave hills (scale bar: 10 µm). (**D**) 3D force microscopy reconstructed monolayer normal force distribution on a 100 µm wave, with wave profile shown below. (**E**) Graph showing the bootstrapped magnitude of calculated forces along the curved profile (purple shaded region). (**F**) Mean bootstrapped normal force vectors along the curved profile (purple shaded region). In (**E**) and (**F**), bootstrapping was performed with 10000 re-samples and the 95 % confidence interval is indicated in the shaded region for each respective color.

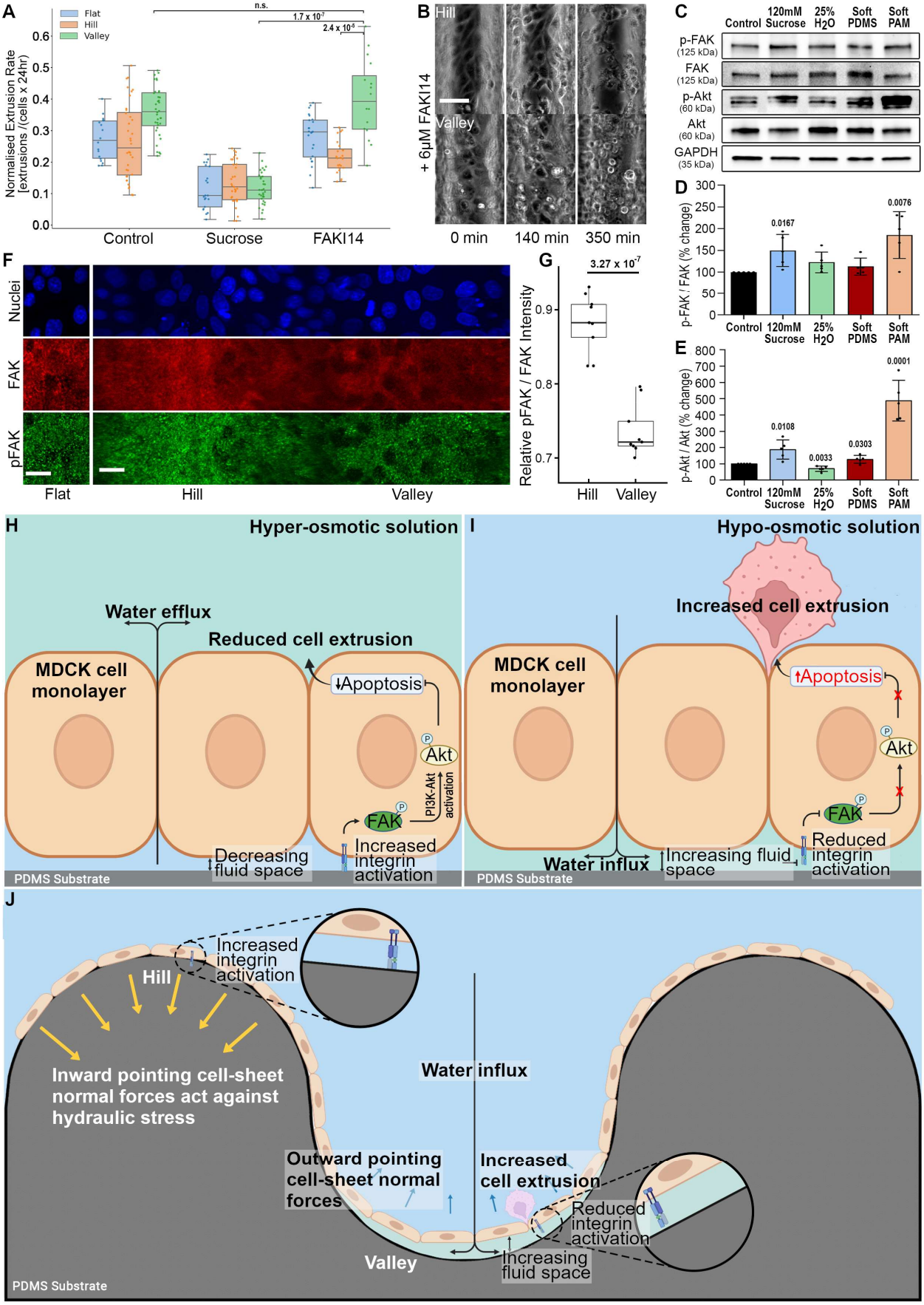
A
Flat
Hill
Valley
n.s.
1.7 x 10-7
2.4 x 10-5
Normalised Extrusion Rate [extrusions /(cells x 24hr)]
Control
Sucrose
FAKI14
B
Hill
Valley
+ 6μM FAKI14
0 min
140 min
350 min
C
Control
120mM Sucrose
25% H2O
Soft PDMS
Soft PAM
p-FAK (125 kDa)
FAK (125 kDa)
p-Akt (60 kDa)
Akt (60 kDa)
GAPDH (35 kDa)
D
p-FAK / FAK (% change)
0.0167
0.0076
E
p-Akt / Akt (% change)
0.0108
0.0033
0.0303
0.0001
F
Nuclei
FAK
pFAK
Flat
Hill
Valley
G
3.27 x 10-7
Relative pFAK / FAK Intensity
Hill
Valley
H
Hyper-osmotic solution
Water efflux
Reduced cell extrusion
MDCK cell monolayer
↓Apoptosis
Akt
PI3K-Akt activation
FAK
Decreasing fluid space
Increased integrin activation
PDMS Substrate
I
Hypo-osmotic solution
Increased cell extrusion
MDCK cell monolayer
↑Apoptosis
Akt
FAK
Water influx
Increasing fluid space
Reduced integrin activation
PDMS Substrate
J
Increased integrin activation
Hill
Inward pointing cell-sheet normal forces act against hydraulic stress
Water influx
Outward pointing cell-sheet normal forces
Increased cell extrusion
Reduced integrin activation
Valley
Increasing fluid space
PDMS Substrate

Fig. 4. Modulation of basal hydraulic stress through media osmolarity and substrate solute permeability regulate cell extrusion via FAK-Akt pathway. (**A**) Cell extrusion rates on 100 μm waves in normal, sucrose, and sucrose + 3 μM FAKI14 media. (**B**) Adding 6 μM FAKI14 leads to cell death that compromised monolayers. Scale-bar: 50 μm. (**C**) Immunoblots of FAK and Akt proteins in MDCK cells subjected to treatments that lead to varying basal hydraulic stresses for 24 hours; namely, iso-osmotic (control), hyper- (4.1 wt. % sucrose), hypo- (25 % water), iso-osmotic with soft PDMS and iso-osmotic with water/solute permeable PAM hydrogel. (**D**) and (**E**) Quantification of the relative expression levels of phosphorylated-FAK (tyr397) as a ratio of p-FAK to total FAK and phosphorylated-Akt (Ser473) as a ratio of p-Akt to total Akt, respectively. GAPDH was used as loading control (M ± SD, n = 5). (**F**) fluorescence images of cell nuclei (false blue), FAK (false red), and p-FAK at tyr397 (false green) on flat, hill and valley; the hill and valley images were unwrapped from 3D stacks. Scale-bar: 20 μm. (**G**) normalized p-FAK/FAK intensities from hill and valley cells. Statistical analysis in table S8. (**H**) and (**I**) Schematic of how osmolarity affect basal hydraulic stress and cell survival. (**J**) Schematic of how curvature induced force differences promote cell survival and death.

Supplementary Materials for

Surface curvature and basal hydraulic stress induce spatial bias in cell extrusion

Cheng-Kuang Huang, Xianbin Yong, David T. She, Chwee Teck Lim

Correspondence to: mbihc@nus.edu.sg (C.-K. H.); ctlim@nus.edu.sg (C. T. L.).

This PDF file includes:

Materials and Methods
Figs. S1 to S6
Tables S1 to S8
Captions for Movies S1 to S19

Other Supplementary Materials for this manuscript include the following:

Movies S1 to S19

Materials and Methods

Microfabrication of periodic cylindrical wave structures

The microfabrication of our hemi-cylindrical wave substrates was, in principle, achieved by first manipulating and fusing multiple glass rods to produce an arrayed template. Then, through a series of molding and surface processing, this template was ultimately replicated in a robust monolithic resin format that can be repeatedly molded with silicone elastomer, or other soft biocompatible material, to create curved surfaces for 3D tissue culture. Although the of molding cylindrical structures to create curved substrates has been attempted *(17, 36)*, our method can achieve very smooth surfaces. This is in contrast with methods that use metal wires *(36)* which, with their considerable machining defects, may contribute to spurious cellular responses. Furthermore, by selectively removing every other rod from the array, we were able to achieve a contiguous wavy landscape that was symmetric in the dimensions of the concave and convex regions.

Figure S1 schematically illustrates in detail the microfabrication procedures involved in producing our cylindrical wave structures. There were essentially 4 major steps in our approach:

Step 1 (fig. S1 a). The first goal was to produce an array of tightly packed uniform glass rods (100 & 200 µm dia., Hilgenberg GmbH, Germany) fixed in place with an UV curable optical adhesive—the Norland Optical Adhesive 73 (NOA73, Norland Products Inc., UK). To facilitate NOA73 lift-off later in the procedure, a glass slide was first pre-treated with Rain-X (800002250, ITW Global Brands, US) according to the manufacturer's instructions. Then, a thin layer of NOA73 was smeared on to the slide followed by the one-by-one placement of glass rods. The quantity of rods will determine the number of periods produced: for example, 10 rods will produce a pattern with 5 periods. Using a sharp needle under an optical microscope, the rods were pushed tightly together, all the while avoiding trapping debris in-between the rods (fig. S1 a i). Minimal amounts of NOA73 should be used to allow surface tension to hold the rods together; excessive NOA73 will cause the rods to drift apart. To hold the rods in position, the array was then pre-fixed under UV illumination for 1 minutes at 25 % power in a UV-KUB 9" (KLOE, France). After this procedure, two spacers of ~1 mm thick were placed on either side of the array (fig. S1 a ii), and additional NOA73 was poured over the array to sufficiently cover it. A second glass slide was used to sandwich the whole construct. This slide was propped up by the spacers and there should be sufficient NOA73 to fill the resulting gap. Again, the NOA73 was cured under UV, this time for 2 minutes at 25 % power. Once the resin has cured, the sandwich construct was pried apart, with separation occurring at the Rain-X treated slide (fig. S1 a iii).

Step 2 (fig. S1 b). With the NOA73 embedded glass rods, we proceed to remove every second rod in the array to create a wave structure symmetric in its concave and convex curvatures. Residual NOA73 on the top side of the array was first cleared away. Specifically, a sharp needle was pushed along the grooves between the rods, from one edge to the other (fig. S1 b i), lifting off resin from these regions. Then, with the same needle, every other rod was gently pried from the edge by wedging the needle tip under the rods. To prevent breaking the delicate rods, rather than lifting them off vertically, the needle was run underneath the length of the rods (fig. S1 b ii). After creating the wave structure, the whole template was gently cleaned using a stiff paint brush, in ethanol followed by water, to remove any NOA73 debris.

Step 3 (fig. S1 c). Due to the finite thickness of the resin between the rods, removing one will unavoidably create a seam along the junctions of neighboring rods (fig. S1 c i inset). To remove these seams, the glass rod wave template was spin coated with a layer of polystyrene cement (3527C, Testors, US) at 1500 RPM 301 for 10 minutes (WS-400BZ-SNPP/LITE, Laurell Technologies, UK). This extra coat of film will however reduce the concave region's dimensions while increasing that of the convex ones. Dimensional symmetry was regained by inverting the

template followed by a second polystyrene spin coat. To perform the inversion, two-part silicone elastomer, polydimethylsiloxane (PDMS Sylgard 184, Dow Inc., US), with cross-linker and monomer mixed in a 1:10 weight ratio, was first molded against the original polystyrene-coated template (fig. S1 c ii). We then created a negative of this PDMS mold by casting against it a second two-part silicone elastomer (Wirosil, BEGO Canada Inc, CA) (fig. S1 c iii). To prevent fusion of the silicones, the PDMS mold was pre-coated with 1 % bovine serum albumin (BSA, A9647-50G, Sigma-Aldrich) reconstituted in Milli-Q water to act as a de-molding layer. An inverted NOA73 wave template was then derived by UV curing fresh NOA73 sandwiched between the Wirosil silicone mold and a glass slide (fig. S1 c iv). The resulting inverted template was subsequently spin coated with a second coat of polystyrene, balancing out the dimensional deviations. This substrate constituted our master wave template.

Step 4 (fig. S1 d). The final step of our procedure was to produce multiple resin clones of the master template. These clones, by virtue of parallel fabrication, will facilitate the scale-up production of wave structures for cell culture. For this, we first create a PDMS mold from the master template (fig. S1 d i). Then, using this mold, NOA73 was repeated cast against it, deriving multiple monolithic NOA73 clones on glass slides (fig. S1 d ii and iii). The clones were subsequently baked at 80 °C for 24 hours before they were used to cast PDMS substrates for cell culture—baking was done to inactivate the adhesion promoter in NOA73 that inhibited PDMS curing. Thereafter, to fabricate wave substrates for cell culture, PDMS was poured onto each clone template and pressed against a large polystyrene culture dish with multiple layers of tape to serve as spacers at either end of the slides (fig. S1 d iv). When cured, the NOA73 templates were pried from the plastic, and the PDMS wave films on the templates were carefully peeled off and attached to 22×22 mm cover-glasses ready for ECM coating (fig. S1 d v and vi).

The above microfabrication procedure was successfully applied to glass rods with diameters down to 100 µm. Due to the unavailability of commercial glass rods with smaller diameters, we developed an augmentative procedure to accomplish wave structure with half periods smaller than 100 µm. Specifically, drawing inspiration from traditional noodle-pulling, silicone molds were lengthwise stretched to obtain narrower waves. The stretched molds were typically fixed in place on a rigid platform with document clips at either ends (fig. S2 a). NOA73 was then used to replicate the stretched mold. To obtain smoother surfaces, this procedure is best performed over several iterations with small stretch increments each time. At each iteration, a new silicone mold was produced from the new narrower wave NOA73 templates to be stretched again (fig. S2 b). Silicone elastomers with larger elongation at breakage than PDMS, such as Wirosil with a 250 % elongation at break, was employed during the stretching procedures. Furthermore, in our case, a 30 % elongation to the mold was applied at each iteration. This derived periodic wave structures with half periods of ∼50 µm after 4 iterations—based on an assumed 0.5 Poisson ratio.

Using the above methods together, wave structures with half periods of ∼200, ∼100, and ∼50 µm were fabricated (main text Fig. 1 A-C). Rectangular waves of similar periodicity to the cylindrical waves were also produced for comparative studies. These structures were fabricated using standard photolithography and soft-lithography *(37)*.

The surface properties of the PDMS wave substrates, as shown in main text figure 1 A-C, were characterized using a scanning electron microscope (JEOL JSM 356 6010LV). Meanwhile, to characterize the dimensions of the structures, cylindrical and rectangular, FITC-collagen I from bovine skin (C4361, Sigma-Aldrich) was coated on some of the samples and then imaged on a confocal microscope (see next section). Figures S3 a-c show orthogonal fluorescence sections of the ∼50, ∼100, and ∼200 µm cylindrical waves, respectively, while S3 d-f show that of the

rectangular waves. Using FIJI and its kappa plugin, the typical dimensions and curvatures (fig. S3 g-h) as determined from the FITC signals were quantified and are tabulated in table S1.

Cell culture, staining and imaging

Madin Darby Canine Kidney type II cells (MTOX1300, ECACC collection purchased from Sigma-Aldrich) were cultured in Minimum Essential Medium (MEM, 11090081, Gibco) supplemented with 5 % FBS (10082147, Gibco), 1× Penicillin/streptomycin (15070063, Gibco), 1× GlutaMax, 1× Sodium Pyruvate (11360070, Gibco), and 1× non-essential amino acids (11140050, Gibco). The cell line was maintained at 37 °C and 5 % CO_2, and subcultured every other day. Cells were typically disposed of before 25 passages.

In order for cells to attach to the PDMS wave substrates, an extracellular matrix coating was required on the surface. This was done by first activating the surface under oxygen plasma for 3 minutes. Then, 500 µl of 20 mM acetic acid solution containing 50 µg of collagen-I from bovine skin (C4243, Sigma-Aldrich) was added to the substrate supported on a 22×22 mm cover-glass and left for 2 hours at room temperature. After this, the collagen-I solution was aspirated and the substrate air dried for 1 hour. The coated substrates were then stored in 4 °C and typically used within a week. Prior to experimentation, coated substrates were re-immersed in 1× phosphate buffered saline (PBS, P4417, Sigma-Aldrich) in a 35 mm culture dish and UV sterilized for 15 minutes in a biosafety cabinet.

To study MDCK responses over the curved substrates, cells were first re-suspended in imaging media (MEM without phenol red, above supplements and 2 % serum) followed by seeding on to the substrates at a density of $\sim 2.5\times10^5$ cells/cm_2. A figure of eight motion was applied to the sample dish to ensure an even distribution of cells. Live-cell microscopy experiments were performed 24 hours after seeding to ensure closure of the monolayer. Otherwise, the monolayers were fixed, at 24, 48 and 72 hours after seeding, for fluorescence imaging.

For nuclei staining, monolayers reaching desired time-points were rinsed in 1× PBS followed by fixing in 4 % formaldehyde (28906, Thermofisher Scientific) for 15 minutes. After two 1× PBS washes, the cells were permeabilized with 0.1 % Triton X-100 (X100, Sigma-Aldrich) for 3 minutes. The cells were then twice washed with 1× PBS, and stained with Hoechst 33342 (H3570, Invitrogen) at 1:1000 dilution. For immunostaining of FAK (610088, BD Transduction Laboratories) and activated FAK (Tyr 397) (AF3398, Affinity Biosciences), cells were first blocked for 30 minutes in 2 % BSA in 1× PBS after permeabilization. The primary antibodies were then diluted 1:400 in the blocking buffer and added to the samples for 2 hours. Afterwards, the samples were rinsed twice in 1× PBS. Secondary antibodies, Alexa Fluor 488 goat anti-rabbit and Alexa Fluor goat anti-mouse (A11008 and A11004, Invitrogen), diluted to 1:400 were then added to the samples and left for another hour. Stained samples were then washed twice in 1× PBS and left in 1× PBS in 4 °C and imaged within a week.

To perform live-cell microscopy, MDCK monolayers grown on substrates attached to cover-glasses were transferred to a stainless-steel cover-glass holder (SC15022, Aireka Scientific, HK) and replaced with fresh image media. The samples were imaged on a Nikon Biostation IMQ, with the cells maintained at 37 °C and 5 % CO_2 through the built-in environmental chamber. Phase contrast z-stack images—13 z-planes for all dimensional conditions—were typically acquired every 7 minutes over 24 hours using the internal 10× objective (0.5 NA) and 1.3-megapixel monochrome camera. Furthermore, to obtain a large field of view, a 3-by-5 overlapping image array was tracked for every time-lapse acquisition.

For imaging fixed and stained samples, these were typically propped up by spacers and mounted upside down in 1× PBS on cover-glasses. These samples were then placed in the same

stainless-steel cover-glass holder (SC15022, Aireka Scientific, HK) used for live-cell imaging. Fluorescence imaging was then performed on a spinning-disk confocal microscope with a Yokogawa CSU-W1 (Yokogawa Electric, Japan) scanner unit attached to a Nikon Ti2-E inverted microscope (Nikon Instruments Inc., US). Fluorophores were excited through the iLAS laser launcher (Gataca Systems, France) containing 405, 488, 561, 642 nm laser lines. Image z-stacks (z-steps=0.3 µm) were imaged with a 40× water immersion objective (CFI Apo LWD 40XWI λS N.A. 1.15, Nikon) and captured with a sCMOS Camera (Prime 95B 22 mm, Teledyne Photometrics, US). The z-positions were precisely controlled by a piezo stage (PI PIFOC Z-stage, Physik Instrumente, US). The whole microscopy system was controlled by the MetaMorph advanced acquisition software (Molecular Devices, USA).

Osmolarity perturbation, drug treatment, and apoptosis detection

To create hyper-osmotic conditions, 4.1 wt. % sucrose, 1 % DMSO, and 0.4 wt. % NaCl were added to the imaging media described in the previous section. Meanwhile, a hypo-osmotic condition was created by adding an extra 25 % Milli-Q water. The osmolarity of each condition was measured using the Vapro vapor pressure osmometer 5520 (Wescor Inc., USA). The measured osmolarities were 403.6 ± 3.8, 418.6 ± 3.5 and 406.3 ± 1.5 mOsm/L (M ± SD, n = 3) for the sucrose, DMSO and NaCl hyper-osmotic conditions. Addition of water resulted in a measured osmolarity of 214.6 ± 4.0 mOsm/L. For comparison, the control iso-osmotic media had an osmolarity of 279.3 ± 3.8 mOsm/L.

To test whether inhibiting focal adhesion phosphorylation at tyrosine 397 was sufficient in rescuing cell extrusion rates in MDCK monolayers in hyper-osmotic conditions, image medium containing sucrose was added with 3 µM FAK inhibitor 14 (SML0837-10MG, Sigma-Aldrich) (from 10 mM stock in water) and replaced the iso-osmotic media used prior to imaging. CellEvent™ (R37111, Invitrogen), a caspase 3/7 substrate that produces fluorescence upon caspase 3/7 activation, was employed to visualize the apoptotic proportion of cell extrusions observed in this study. One drop of the reagent was added to 500 µL of medium one hour before live-cell imaging. To minimize phototoxic effects, only four regions, each with 3 z-steps, were imaged for each sample.

To buffer against any increases in hydraulic stress, polyacrylamide hydrogels were fabricated. Specifically, a master polyacrylamide mix was then generated by mixing 200 µl of 40 % polyacrylamide solution (Bio-Rad), 200 µl of 2 % bis-acrylamide solution, 580 µl of the MilliQ water and 1.5 µl of TEMED. Next, to 150 µl of the master mix, 2 µl of 10 % APS was added and mixed using a vortex. This was then added onto the NOA73 molds described in the previous sections before a cover-glasses was placed on top of the mold. The polyacrylamide was allowed to gel for 30 minutes.

To ensure that the polyacrylamide gel binds to the cover-glasses, the cover-glasses were previously treated with a solution containing 2 % trimethoxysilyl propyl methacrylate (Sigma-Aldrich) and 1 % glacial acetic acid in absolute ethanol for 10 minutes. The cover-glasses were then washed 3× in absolute ethanol before being dried in an oven at 80 °C for 2 hours.

The mold was then separated from the glass cover-glasses and the polyacrylamide gel. This process was done under PBS to ensure that the polyacrylamide gel separates cleanly. The polyacrylamide gel was subsequently washed 3× with PBS before being stored in PBS at 4 °C overnight.

The collagen coating procedure for these hydrogel substrates is described in the 3D force microscopy section.

Analysis of extrusion rates

Imaging of the various substrates resulted in multiple 3D time-lapse image stacks. To facilitate the downstream analysis of these image stacks, they were unwrapped to obtain a 2D representation of the monolayer. Unwrapping was done by first drawing the side profiles of the wave structures manually. A coordinate map, which detailed the correspondence of the coordinates in 3D space to the 2D plane, was generated from these side profiles. This was then used to unwrap the 3D image stack via spline interpolation.

Neural network to detect extrusion events. An attention gated residual U-net was trained to detect extrusion events (fig. S5 a). The backbone of the encoder and decoder arms of the network followed that laid out previously in *(38)* with the following modifications. The residual block was modified using the ResNet-D block *(39)* with pre-activation *(40)* and the addition of the Squeeze-and-Excitation block *(41)*. Furthermore, spatial attention gates were used on the long connections between residual blocks *(42)*. Due to the inherent class imbalance between the background pixels and the pixels corresponding to the extrusion events, the symmetric unified focal loss was used *(43)*. Deep-supervision was performed for the various image scales by adding a 1×1 convolution block after each group of residual blocks *(44)*. The ground truth was scaled down to the appropriate size and the same loss function as the full-sized ground truth was used. Spatially varying labelling smoothing was applied to the ground truth image as well as every deep-supervision level to mitigate overconfidence in the network *(45)*.

Training of the network was performed for a total of 200000 training steps with each step having a batch size of 32. The initial number of filters was set at 64. A cosine learning rate decay, which started from an initial learning rate of 5×10^{-4} and decayed to a minimum of 1×10^{-6}, was employed as suggested in *(46)*. The training data consisted of input images with 5 frames, 2 before and 2 after the frame of interest, along with hand annotated mask of the extrusion events (fig. S5 b). The intensity of the input images was normalized using percentile normalization. These images were initially 192×192 pixels^2 in size and were subsequently cropped to the final size of 128×128 pixels^2 after data augmentation. Both positive and negative examples were annotated to ensure that only extrusion events were being identified by the network. The following data augmentation were used — flips (horizontal and vertical), transpositions and random rotations (multiples of 90°).

As the extrusion process can occur over a few frames, further downstream processing was done to identify the start of the extrusion event. First, a size filter was used to filter out any small objects smaller than 80 pixel^2. Holes smaller than 80 pixel^2 were filled as well. Objects with an eccentricity > 0.95 and solidity > 0.5 were also removed. Next, the centroid locations of all the objects were calculated. Objects in different frames were determined to belong to the same extrusion event if the distance between the two centroids were less than 20 pixels and the time difference was less than 5 frames. The first instance of the object in each event was used to represent the position and time of the extrusion. Lastly, only extrusions that occur within the region of interest and the 24-hour timeframe were included in the extrusion rate calculation. The normalized extrusion rate was then calculated by dividing the extrusion rate from each image with the initial cell density for that sample.

Estimation of cell density. Estimation of cell density was done using the StarDist network *(47)*. Briefly, training images were prepared by hand drawing labels for the cells in representative images using Fiji. The images were also pre-processed using a log-contrast filter to normalize the contrast of the images. The following augmentations were used to augment the training data – random rotation (multiples of 90°), transpositions (horizontal and vertical), flip, motion blur, median blur and Gaussian blur. The training data was also randomly cropped to the final size of 256×256 px before being fed into the network. The default parameters for the StarDist network were used except for the number of epoch and iterations per epoch which were set to 1000 and 100 respectively. Prediction of new images were done using the network weights that provided the

smallest loss value during training. By passing the first frame of the time-lapse through the network, the number of cells, and consequently the cell density, were determined for each predefined region of interest (fig. S5 d). The average initial cell density was then calculated for each sample.

Statistical analysis. A total of 3 samples, comprising of 12 images each, were obtained for every condition except for the control which has 4 samples. Statistically analysis of the normalized extrusion rate was performed on these regions of interest using the Python statsmodels module. Two-way ANOVA was performed using the type III sums of squares as well as the HC3 heteroskedasticity-consistent standard error estimators. If the interaction term was significant, the main effects were ignored and only the simple main effects were considered. One way ANOVA of the simple main effects was then performed if multiple comparison were made during post hoc testing. Two-tailed Welch's unequal variances T-test were conducted to determine if any of the comparisons were significant. The Benjamini-Hochberg procedure was performed if multiple comparison were made. Normality of the data was verified via visual inspection of the Q-Q plot and histogram of the residuals. Effect sizes were calculated via bootstrapping with 10000 resamples and presented as the 95% confidence interval.

3D force microscopy

Preparation of 3D force microscopy substrate. To study the forces generated by the cells grown on the curved substrates, polyacrylamide substrates with fluorescent beads evenly dispersed throughout the substrate were fabricated (fig. S6 a, d). Specifically, an aliquot of 10 µl of 0.2 µm fluorescent (580/605) carboxylated microspheres (F8810, Invitrogen) was added to 9.5 ml of Milli-Q water and sonicated for 10 minutes. This solution was then filtered using a 0.45 µm syringe filter (Sartorius). A further 0.5 ml of 500 mM of MES buffer, pH 6.0, was added to the filtered solution. The steps to fabricate the polyacrylamide gel were followed as described in previous sections except for the 580 µl of filtered bead solution being used instead of Milli-Q water.

Culturing of cells for 3D force microscopy. To allow for the MDCK cells to attach to the polyacrylamide gel, the surface was coated with collagen-I from bovine skin (C4243, Sigma-Aldrich). This was achieved by functionalizing the gel surface using sulfosuccinimidyl 6-(4'-azido-2'-nitrophenylamino) hexanoate (sulfo-SANPAH). Specifically, 40 µl of 0.2 % acetic acid was added to 2 µl of 0.02 mg/ml sulfo-SANPAH that had been previously dissolved in DMSO. This solution was then added to the polyacrylamide gel surface. A silicone block was used to mechanically agitate the solution to ensure even distribution of the sulfo-SANPAH. UV treatment of the sulfo-SANPAH was done using a UV-KUB 9 (KLOE, France) at 6 % power for 5 minutes. The gel was then washed 3× in 0.2 % acetic acid. This process was repeated a second time with fresh sulfo-SANPAH. Finally, the gel was washed 3× with PBS. 400 µl of PBS containing 50 µg of collagen-I was aspirated onto the gel surface. The collagen was left for 2 hours at room temperature with occasional mixing with a pipette to prevent any collagen gel formation. The gel was then washed 3× with PBS before being stored in PBS. Cell seeding was performed as described previously. After the cell have initially started to attach, the gel was cut using a sharp blade until a small region of interest of approximately 5×1 mm was left (fig. S6 b). The cells were then allowed to grow for 24 hours until a full monolayer was formed (fig. S6 c, e).

Imaging setup. To image the bead displacements, the gel containing cover-glasses were transferred to stainless steel cell culture vessels and 500 µl of the original media, in which the cell was previously growing in, were added. The vessels were sealed using a custom-made lid to ensure proper humidity control. Imaging of the beads were done using the same imaging system previously used for fixed cells. A z-step size of 0.275 µm was used to ensure that the voxel size

was the same for all dimensions. Two sets of fluorescent bead images were captured. The first set consist of a z-stack of the beads that was captured with the cell still attached to the gel. The second set consisting of a time-lapse of 5 frames at 15-minute intervals was captured after the cell were removed using 100 µl of sodium dodecyl sulfate (SDS) solution. The SDS solution was prepared by diluting 10 % SDS using the original media to reach a final concentration of 1 %. To minimize any gel deformation, an additional 250 µl of Milli-Q water was added per 1 ml of SDS solution to minimize any gel volume changes due to the addition of SDS. A representative bright-field image of the cells and projected side profile of the fluorescent beads before and after SDS treatment are shown in fig. S6 f and g respectively.

3D displacement estimation. The displacement of the beads was determined using the two-frame 3D Farneback optical flow method *(48)*. A CUDA accelerated implementation was written in Python to speed up the computational time required for displacement estimation. The following parameters for the algorithm were used: 5 iterations, 5 pyramid levels with a scaling factor of 0.5, kernel size of 7 px and box filter size of 31 px. The images were pre-processed by aligning the two sets of images manually before being smoothed with a Gaussian filter of radius 7 px. Validation of the estimated displacement were done by using the estimated displacements to generate a pixel map. This pixel map was used to map the pixels from the bead image without any cells. Qualitative validation was then performed by visually inspecting if there were reasonable alignment between this mapped image and the bead image with cells (fig. S6 h). Post processing of the estimated vectors were done as followed. First, a suitable region deep in the substrate was chosen and the median x and y displacement from this region was used to eliminate any residual displacement in x and y due to misalignment of the two images. Second, the z displacements along the cross section of the hill were fitted using a best fit line to obtain the z displacement correction function. This function would adjust for any misalignment in z as well as gel shape changes in z because of minor changes to the salt concentration. Last, displacements outside the region of interest were set as undefined.

3D force calculation. The calculation of forces from the displacements were treated as a linear inverse problem. Here, the output (calculated displacements, fig. S6 i) and the system were known, while the input (force exerted by the cells) needed to be computed. The system could be obtained from finite element modelling of the gel. The shape of the gel was obtained by subdividing the image into smaller 3D subsets along the axis perpendicular to the feature. Binarization of the image was preformed and the centroid location of the beads were obtained for each subset. The centroid locations were then projected along the axis perpendicular to the feature to obtain a representation of the points on a 2D plane. The alpha shape of the 2D plane was then determined and the outlines for the alpha shapes from each subset were used to calculate the 3D representation of the gel using the "Blend" tool in Ansys Student SpaceClaim 2021 R1 (Ansys Inc, USA). The 3D representation was meshed using Ansys Student Workbench 2021 R1 with the top face having a maximum element edge length of 5.5 µm (fig. S6 j). The bottom face was set using the zero-displacement boundary condition. To account for any edge effects, the symmetric boundary condition was set for all the faces except for the top and bottom faces. The material properties were specified with a Young's modulus of 30 kPa and a Poisson's ratio of 0.457. For each node on the top surface of the mesh, a nodal force of 1×10^{-8} N was applied to the x, y, and z directions sequentially and the corresponding nodal displacement of all the nodes was then recorded. The nodal displacements were then arranged into a matrix describing the response of the system to various nodal forces. The calculated displacements were also mapped to the various nodal positions to obtain the outputs at each node. The inverse problem was then solved via regularization using the Tikhonov method with the regularization parameter determined using the

L-curve method. The surface force per unit area was subsequently calculated by taking the average force of a node and its neighbors and dividing it by the area covered by the nodes (fig. S6 k).

Analysis of 3D forces. For each node, the Gram-Schmidt process was used to obtain the orthonormal vectors with the z axis being the normal vector relative to the tangent plane of the node, the y axis being the vector along the long axis of the wave structure and the x axis being the direction that follows along the curvature. Each force was then re-expressed using their respective orthonormal vectors. As cylindrical waves were used, the position of each node can also be expressed as the convex central angle form by the node and a horizontal line cutting across the center of the circle. The bottom of the valley would thus have an angle of $-\pi/2$ rad while the top of the hill would have a value of $\pi/2$ rad. The interface would have an angle of 0 rad. This facilitated the comparison between the 3 different sizes. The angles were then binned to facilitate the calculation of the mean value as well as the bootstrapped 95% confidence interval. A total of 10000 resamples were used in the calculation of the 95% confidence interval. A total of 6 samples were obtained for the 100 µm waves while 3 samples were obtained for the 50 and 200 µm samples.

Reflection interference contrast microscopy

RICM experimental setup. In order to demonstrate the accumulation of water at the basal side of an epithelial monolayer, MDCK monolayers on glass were transferred to stainless steel culture vessels after 24 hours. However, instead of replenishing with iso-osmotic image media described previously, a hyper-osmotic MEM with sucrose was used. Moreover, as the samples were tightly sealed to prevent osmolarity shifts due to evaporation, MEM with Hank's balanced salt was adopted as the base medium here (11575032, Gibco). After conditioning the cells in hyper-osmotic medium for 4 hours at 37 °C, an air-tight lid was placed on the sample holder. Reflection interference contrast microscopy (RICM) was performed on a Nikon A1R laser scanning confocal microscope operating in reflection mode using 640 laser excitations. The cell-to-substrate attachment was tracked over a 5-hour period with an iso-osmolarity rescue (adding water) performed halfway. The whole system was maintained at 37 °C. The Nikon Perfect Focus System was activated to account for stage drift over time. Furthermore, z-stacks with a 4 µm range and 200 nm intervals were typically acquired to ensure the data always contained the reflection plane of interest.

RICM was also employed to highlight the difference between cell-to-basal attachments between MDCK monolayers on the hills and valleys of the wave substrates. To improve the contrast of RICM, the cells were cultured on wave substrates made from the higher refractive index NOA73 instead of PDMS. After 24 hours, the medium was replenished with iso-osmotic image medium with Hank's balanced salt, and similarly conditioned for 4 hours prior to imaging. Due to the large vertical span of the structures, the features (hill, valley, and flat) were imaged separately. Typically, z-stacks were acquired with a 20 µm range and 200 nm intervals around the apex of geometries (applicable to hills and valleys only). These values where chosen as RICM would have failed in regions where the surfaces become vertical.

RICM data analysis. Our RICM data comprised of z-stacks taken over time and/or over regions. As RICM images are brightest when the plane of reflection is in focus, the reflecting plane at which cells meet the surface were extracted by performing maximum projection in ImageJ (main text Fig. 2 C, D and G). Furthermore, being the closest objects to the substrates, focal adhesions should exhibit the lowest intensities *(25, 26)*. Utilizing this property, we effectively removed fluctuating backgrounds across time frames by left-shifting the histograms of each frame such that all the minima aligned at zero. This allowed us to register the changing intensities—i.e., the cell-substrate basal separation—over time more accurately (main text Fig. 2 E). Then, to derive a quantitative comparison, the medians of the grey values were averaged over the duration of the

treatments (hypo-osmotic or iso-osmotic). Average medians from 3 independent regions and 3 independent samples were compiled 687 (Main-Text Fig. 2f). Normality and equal variance were analyzed using Shapiro-Wilk test and Levene's test, respectively. Statistical significance was calculated using two-tailed paired student's t-test. Effect size was calculated using Cohen's d.

To make intensity comparisons between cells on the flat, hill and valley regions, rectangular region of interests of 12×150 µm were first randomly selected from the max-projected z-stacks of each feature. Based on similar reasoning, the histogram minima were left-aligned to zero grey value. Quantitative comparisons were facilitated through the extraction of median grey values from the aligned histograms—3 independent region of interests for each feature, and from 4 independent samples (main text Fig. 2 H). Normality and equal variance were analyzed using Shapiro-Wilk test and Levene's test, respectively. Statistical significance was determined using 1-way ANOVA followed by Tukey HSD post hoc test. Effect size was calculated using Cohen's d. All data analysis in this section was performed using the statistical programming software, R.

Fluorescence intensity analysis

FAK phosphorylation intensity analysis. Due to the 3D nature of our wave substrates, differences in the raw intensities of phosphorylated focal adhesion kinase (p-FAK) fluorescence between hill and valley cells cannot be used directly. To eliminate differences contributed by optical scattering through the material as well as variations in staining, we normalized hill and valley p-FAK and total FAK median grey values against the average median values obtained from 3 random flat regions of the same sample. Then, the p-FAK/FAK ratio, from 3 independent regions and 3 independent samples was calculated and compiled (main text Fig. 4 G). Normality and equal variance were analyzed using Shapiro-Wilk test and Levene's test, respectively. The two-tailed student's t-test was used to calculate the significance in the relative activation of p-FAK between cells on the hills and those in the valleys. Effect size was calculated using Cohen's d. All data analysis in this section was performed using the statistical programming software, R.

Immunoblot Analysis

Preparation of MDCK cell lysates. For each experimental condition, the attached MDCK cells were collected by trypsinization (TrypLE Express, Thermo Scientific) supplemented with 50 mM EDTA (Thermo Scientific). The cell pellets were then lysed in radioimmune precipitation assay (RIPA) buffer (Thermo Scientific) containing 25 mM Tris-HCl, pH 7.6, 150 mM NaCl, 1 % NP-40, 1 % sodium deoxycholate, 0.1 % sodium dodecyl sulfate (SDS), along with a protease and phosphatase inhibitor cocktail (Halt™, dilution: 1:100, Thermo Scientific). The lysates were centrifuged at 13,000 rpm for 15 minutes at 4 °C to separate the cell debris from the protein-rich supernatant. The supernatants were then collected into fresh tubes, and protein concentrations were determined by bicinchoninic acid (BCA) assay kit (Thermofisher Scientific) as per manufacturer's instructions.

Immunoblotting. Protein samples were added with equal volume of 2× Laemmli sample buffer (Bio-Rad Laboratories, Hercules, CA, USA) containing 65.8 mM Tris-HCl, pH 6.8, 2.1 % SDS, 26.3 % (w/v) glycerol, 0.01 % bromophenol blue and supplemented with 200 mM dithiothreitol (DTT, Merck). The resultant mixtures were then denatured at 95 °C for 7 minutes and cooled to room temperature. The denatured protein samples (20 µg) were then separated on 4-20 % SDS-polyacrylamide gels using a Tris-glycine running buffer (Bio-Rad) and electroblotted onto nitrocellulose membranes (0.2 µm pore size, Bio-Rad) using a wet Criterion blotter (Bio-Rad) in transfer buffer containing 25 mM Tris base, 150 mM glycine, and 20 % (v/v) methanol for 1 hour at 100 V. The membranes were then incubated in blocking buffer, consists of 5 % (w/v) bovine serum albumin (BSA, Hyclone) in Tris-buffered saline (1× TBST, containing 20 mM Tris-

HCl, pH 7.5, 137 mM NaCl and 0.2 % Tween-20) for 1 hour at room temperature to minimize non-specific binding. The membranes were then incubated for 24-48 hours at 4 °C in antibodies targeting the following proteins (dilution factors, incubation duration and manufacturer's catalogue numbers are in table S7): FAK, phosphorylated-FAK (Tyr397), Pan-AKT, phosphorylated-AKT (Ser473) and GAPDH diluted in blocking buffer. After three washes with 1× TBST, the membranes were incubated in either horseradish peroxidase (HRP)-conjugated goat anti-rabbit IgG (dilution: 1:3000, CST cat# 7074) or horse anti-mouse IgG (dilution factor 1:3000, CST cat# 7076) diluted in blocking buffer for 1 hour at room temperature. The membranes were then subjected to peroxidase-based detection by using enhanced chemiluminescence (ECL) detection reagent (Clarity Max™ Western ECL Substrate, Bio-Rad), and the chemiluminescent signals were visualized by ChemiDoc Touch System (Bio-Rad) and captured by Image Lab software (v 5.2.1). Protein levels were quantified by densitometric analysis using ImageJ software (v 1.53o, National Institute of Health, 755 USA).

Statistical analyses. Statistical analyses of all data in this section were performed using two-tailed Student's t-test to determine the differences between treatment groups and control group. GraphPad Prism software (v 6.01, GraphPad Software, Inc, La Jolla, CA, USA) was used for these analyses.

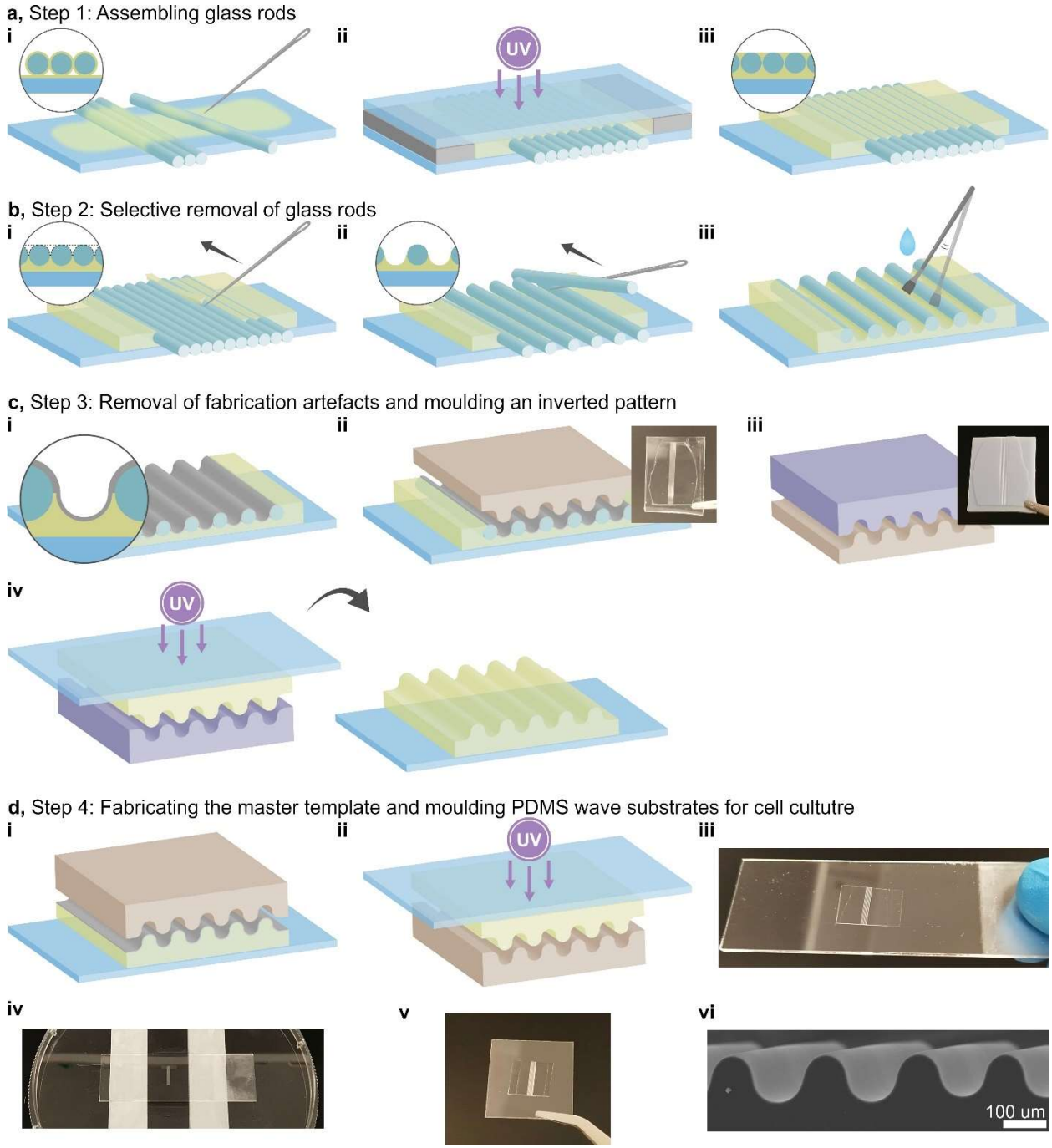

Fig. S1.

Schematic diagram showing the steps for microfabricating smooth periodic hemi-cylindrical wave substrates using glass rods and iterative molding.

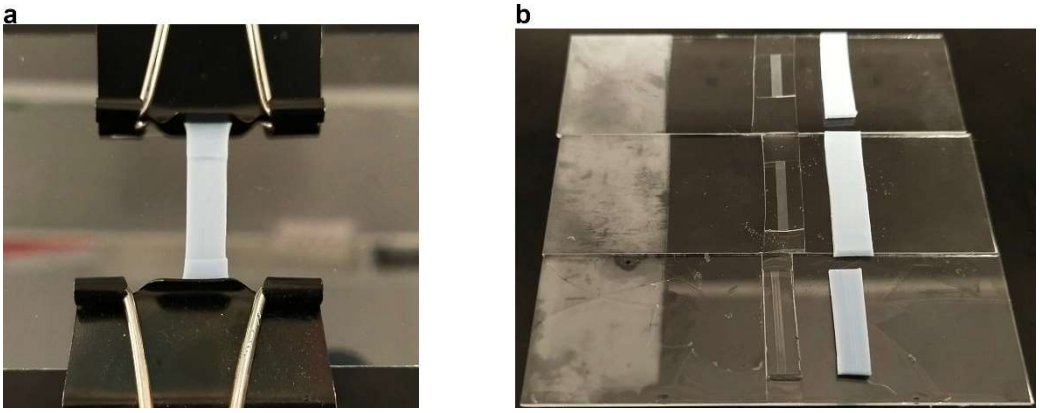

Fig. S2.

Demonstration of achieving dimensions smaller than commercially available glass rods using an iterative stretching and molding method. a, a stretchy silicone with wave pattern was held stretched for optical curable resin casting. **b**, a subsequent stretchy silicone was molded against the new resin template created from **a**; the whole process was repeated until the desired reduction in dimension was reached.

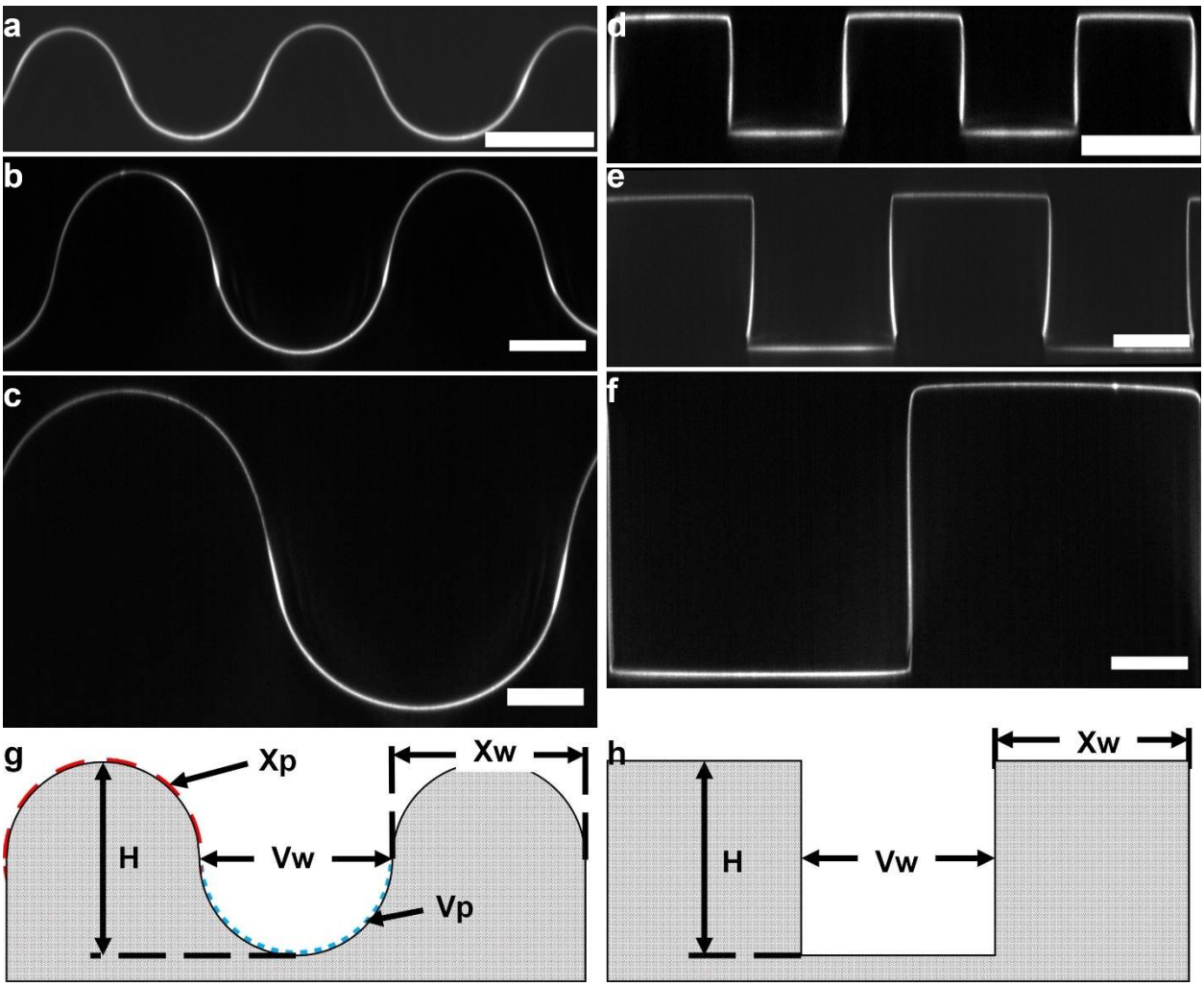

Fig. S3.

Dimensional characterization of cylindrical and rectangular waves through fluorescent collagen I z-stacks. a-c, 50, 100, and 200 µm cylindrical waves. **d-f**, 50, 100, 200 µm rectangular waves. Scale-bars = 50 µm. **g and h**, dimensions measured: curvature (Xp and Vp); width (Xw and Vw); and height (H). Values tabulated in table S1.

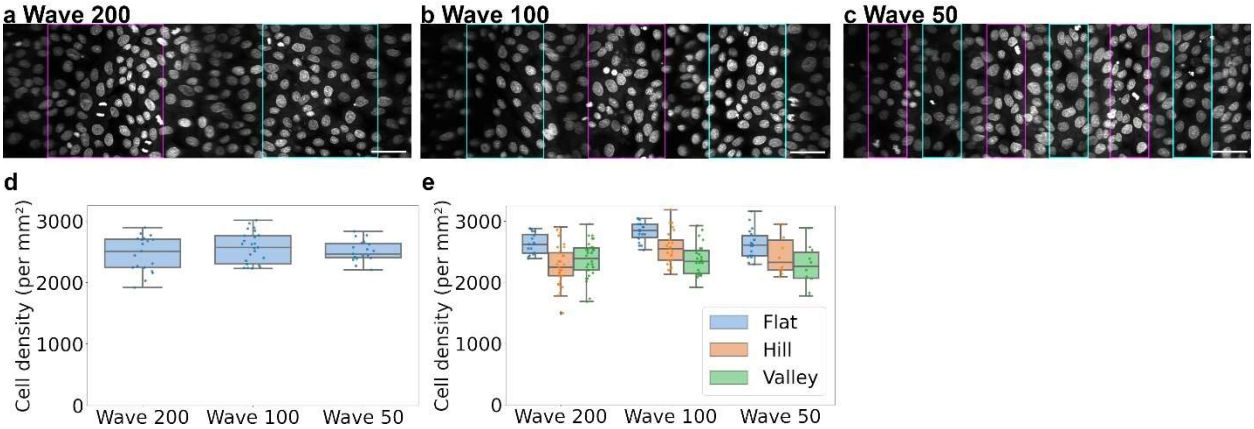

Fig. S4.

Analysis of cell density 24 hours post seeding. a-c, surface unwrapped fluorescent z-stacks of Hoechst stained MDCKs on 200, 100 and 50 µm waves. Hills: cyan boxes and Valleys: magenta boxes. Scale-bars: 50 µm. **d**, boxplot of overall cell densities, determined from nuclei staining, across wave dimensions at the initial time point. **e**, cell densities in **d** plotted according to curvature type.

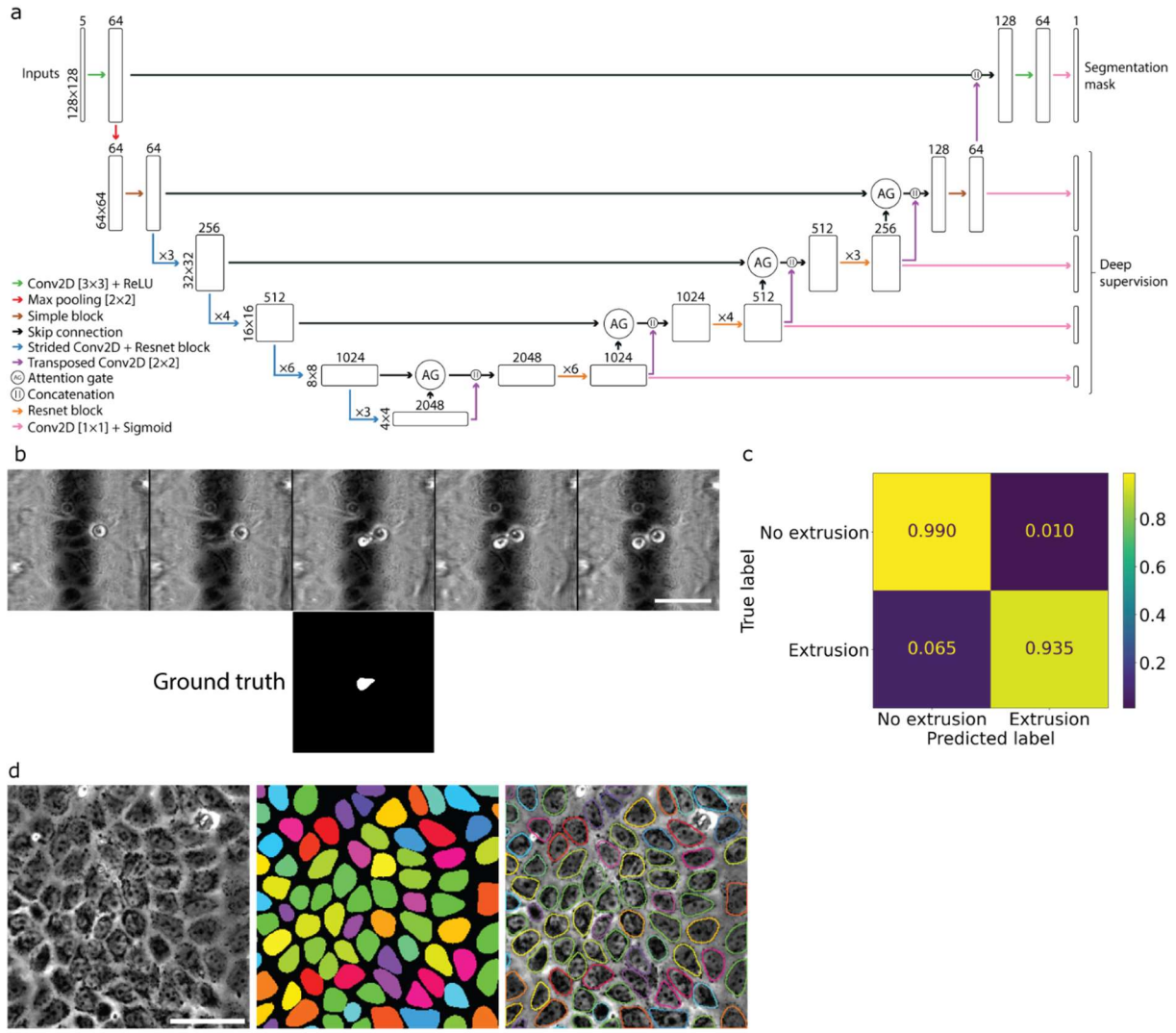

Fig. S5.

Calculation of the normalized extrusion rate. a, architecture of the attention-gated residual U-Net. **b**, example of a manually annotated extrusion event using the sequence of 5 timeframes above and the ground truth binary mask below. **c** confusion matrix of the machine learning network. **d**, Left: bright-field image; Center: prediction from StarDist; Right: overlay of the prediction outline on the bright-field image. Scale-bars: 50 µm.

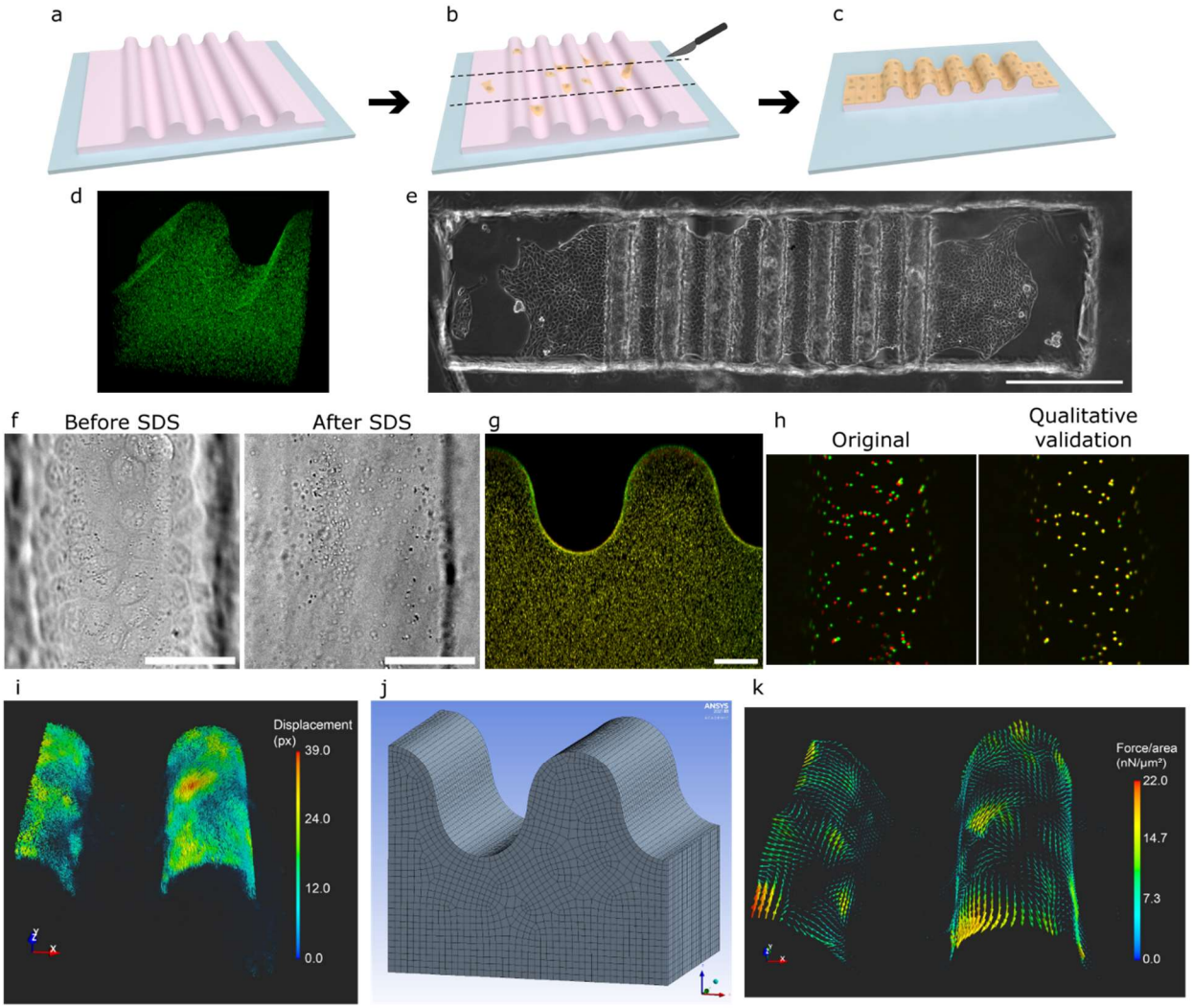

Fig. S6.

3D force microscopy. a-c, schematic for the preparation of the gel as well as the cell seeding process. **d**, 3D-view showing the even distribution of fluorescent beads in the polyacrylamide gel. **e**, bright field image showing the cut get and the monolayer of cells on the curved substrate. Scale-bar: 500 µm. **f**, bright field images showing the removal of cells through the addition of 1 % SDS. **g**, maximum projected side profile of the polyacrylamide gel before (red) and after SDS treatment (green). **h**, Qualitative validation of the calculated displacements. Left: original fluorescent image showing the bead locations with cells (red) and without cells (green). Right: overlay of the mapped image (green) and the bead image with cells (red). **i**, 3D-view of the calculated displacements obtain using the two-frame 3D Farneback optical flow method. **j**, Representative 3D structure and mesh used in the finite element modelling of the polyacrylamide structure. Image used courtesy of ANSYS, Inc. **k**, 3D-view of the average nodal force obtain by solving the inverse problem. Scale-bars: 50 µm unless otherwise stated.

Substrate type	Profile curvature (mean +/- SD μm^{-1})	Curvature variance (mean +/- SD μm^{-2})	Profile width (mean +/- SD μm)	Total height (mean +/- SD μm)
50_cyl (concave region)	0.0306 +/- 0.0016	0.0163 +/- 0.0010	63.6 +/- 3.4	53.5 +/- 5.1
50_cyl (convex region)	0.0362 +/- 0.0028	0.0218 +/- 0.0019	49.5 +/- 3.3	
100_cyl (concave region)	0.0173 +/- 0.0003	0.0092 +/- 0.0008	112.1 +/- 0.8	119.0 +/- 0.4
100_cyl (convex region)	0.0174 +/- 0.0011	0.0102 +/- 0.0020	104.9 +/- 0.6	
200_cyl (concave region)	0.0107 +/- 0.0005	0.0071 +/- 0.0008	197.6 +/- 4.6	209.3 +/- 3.4
200_cyl (convex region)	0.0105 +/- 0.0008	0.0068 +/- 0.0011	190.7 +/- 3.4	
50_rec (groove)	-	-	47.1 +/- 1.2	43.0 +/- 1.6
50_rec (ridge)	-	-	47.5 +/- 0.4	
100_rec (groove)	-	-	97.4 +/- 1.1	97.3 +/- 4.3
100_rec (ridge)	-	-	101.8 +/- 2.2	
200_rec (groove)	-	-	190.8 +/- 1.4	187.3 +/- 0.7
200_rec (ridge)	-	-	193.2 +/- 2.4	
For comparison, curvatures of 50 , 100, and 200 μm circles are 0.04, 0.02, and 0.01 μm^{-1} respectively				

Table S1.
Table of cylindrical and rectangular wave dimensions.

a

Source of variation	Sum of squares	DOF	Mean square	F	p-value
Intercept	0.958	1	0.958	84.310	8.035×10^{-18}
Curvature	0.004	1	0.004	0.330	5.664×10^{-1}
Size of feature	0.824	5	0.165	14.508	1.061×10^{-12}
Interaction	0.415	5	0.083	7.297	1.849×10^{-6}
Within	3.318	292			
Total	5.519	304			

b

Group	Sample 1	Mean	Std	Sample 2	Mean	Std	Difference	DOF	Welch T	p-value	95% Cohen D
Wave 50	Valley	0.325	0.082	Hill	0.187	0.067	0.138	44.2	6.374	9.372×10^{-8}	[1.144, 2.348]
Wave 100	Valley	0.308	0.094	Hill	0.206	0.071	0.103	35.5	3.893	4.187×10^{-4}	[0.360, 1.857]
Wave 200	Valley	0.195	0.099	Hill	0.213	0.111	-0.018	45.3	-0.586	5.605×10^{-1}	-
Rec 50	Valley	0.359	0.114	Hill	0.418	0.132	-0.059	56.8	-1.852	6.922×10^{-2}	-
Rec 100	Valley	0.295	0.041	Hill	0.226	0.066	0.069	38.5	4.364	9.274×10^{-5}	[0.627, 1.739]
Rec 200	Valley	0.282	0.099	Hill	0.270	0.184	0.012	44.5	0.306	7.607×10^{-1}	-

Table S2.

Tables of statistical analysis on varying structure sizes and curvatures. a, 2-way ANOVA analysis to determine if curvature and size of structure have an effect on the normalized extrusion rates. **b**, Post hoc t-test statistics for the comparisons made with regard to the different sizes of structures.

a

Source of variation	Sum of squares	Degrees of freedom	Mean square	F	p-value
Intercept	1.630	1	1.630	291.835	4.906×10^{-50}
Curvature	0.137	2	0.069	12.265	6.663×10^{-6}
Osmolarity	1.405	5	0.281	50.311	8.791×10^{-41}
Interaction	0.334	10	0.033	5.981	1.701×10^{-8}
Within	2.340	419			
Total	5.847	437			

b

Simple effect	Source of variation	Sum of squares	DOF	Mean square	F	p-value
Hill	Osmolarity	2.220	4	0.555	70.846	4.689×10^{-33}
	Within	1.128	144			
	Total	3.349	148			
Valley	Osmolarity	2.017	4	0.504	138.930	2.150×10^{-48}
	Within	0.523	144			
	Total	2.539	148			
Flat	Osmolarity	0.985	4	0.246	60.805	1.200×10^{-22}
	Within	0.300	74			
	Total	1.284	78			
Control	Curvature	0.222	2	0.111	12.265	2.031×10^{-5}
	Within	0.786	87			
	Total	1.008	89			
PBS	Curvature	0.075	2	0.037	5.446	6.846×10^{-3}
	Within	0.390	57			
	Total	0.465	59			
Sucrose	Curvature	0.005	2	0.003	0.740	0.480
	Within	0.311	84			
	Total	0.317	86			
DMSO	Curvature	0.026	2	0.013	2.961	0.059
	Within	0.290	67			
	Total	0.315	69			
NaCl	Curvature	0.007	2	0.004	1.097	0.340
	Within	0.223	67			
	Total	0.230	69			
Water	Curvature	0.091	2	0.045	7.594	1.192×10^{-3}
	Within	0.340	57			
	Total	0.431	59			

c

Group	Sample 1	Mean	Std	Sample 2	Mean	Std	Difference	DOF	Welch T	Adj. p-value	95% Cohen D
Hill	Control	0.267	0.120	PBS	0.283	0.087	-0.016	57.6	-0.602	5.496×10^{-1}	-
				Sucrose	0.134	0.067	0.133	55.8	5.758	6.296×10^{-7}	[0.961, 1.867]
				DMSO	0.119	0.073	0.148	59.1	6.075	2.423×10^{-7}	[1.000, 2.004]
				NaCl	0.141	0.072	0.126	58.5	5.213	3.170×10^{-6}	[0.787, 1.808]
				Water	0.470	0.093	-0.203	56.6	-7.383	3.822×10^{-9}	[-1.384, -2.513]
Valley	Control	0.361	0.077	PBS	0.355	0.080	0.005	48.4	0.252	8.023×10^{-1}	-
				Sucrose	0.117	0.051	0.243	60.8	15.572	1.395×10^{-22}	[3.102, 4.635]
				DMSO	0.090	0.055	0.271	61.6	6.344	1.821×10^{-23}	[3.213, 5.112]
				NaCl	0.165	0.045	0.196	57.7	12.694	3.210×10^{-18}	[2.446, 3.866]
				Water	0.389	0.064	-0.029	55.2	-1.558	1.248×10^{-1}	-
Flat	Control	0.273	0.066	PBS	0.282	0.080	-0.009	20.5	-0.310	7.599×10^{-1}	-
				Sucrose	0.115	0.065	0.158	36.0	7.504	2.895×10^{-8}	[1.846, 3.352]
				DMSO	0.137	0.070	0.136	27.3	5.611	5.762×10^{-6}	[1.316, 3.104]
				NaCl	0.162	0.048	0.111	29.9	5.497	5.762×10^{-6}	[1.319, 2.780]
				Water	0.457	0.065	-0.184	24.0	-7.527	1.838×10^{-7}	[-1.864, -4.412]
Control	Hill	0.267	0.120	Flat	0.273	0.066	-0.007	51.4	-0.262	7.940×10^{-1}	-
	Valley	0.361	0.077	Flat	0.273	0.066	0.087	39.4	4.313	3.139×10^{-4}	[0.656, 1.863]
	Valley	0.361	0.077	Hill	0.267	0.120	0.094	59.9	3.945	3.174×10^{-4}	[0.458, 1.499]
PBS	Hill	0.283	0.087	Flat	0.282	0.080	0.001	23.8	0.027	9.787×10^{-1}	-
	Valley	0.355	0.080	Flat	0.282	0.080	0.073	22.0	2.591	2.498×10^{-2}	[0.243, 1.807]
	Valley	0.355	0.080	Hill	0.283	0.087	0.073	45.7	3.015	1.256×10^{-2}	[0.332, 1.547]
Water	Hill	0.470	0.093	Flat	0.457	0.065	0.013	30.0	0.495	6.241×10^{-1}	-
	Valley	0.389	0.064	Flat	0.457	0.065	-0.068	21.9	-2.954	1.104×10^{-2}	[-0.327, -2.069]
	Valley	0.389	0.064	Hill	0.470	0.093	-0.081	40.9	-3.506	3.356×10^{-3}	[-0.539, -1.590]

Table S3.

Tables of statistical analysis on varying media osmolarities. a, 2-way ANOVA analysis to determine if osmolarity and curvature have an effect on the normalized extrusion rates. **b**, 1-way ANOVA of the simple effects on the normalized extrusion rates. **c**, Post hoc t-test statistics for the comparisons made with regard to the various experimental conditions.

a

Statistics of median RICM intensities over hypo- and iso-osmotic treatment time-frames.

	Statistics			Two-tailed Paired t-test					Cohen D		
Condition	N	Mean (grey value)	SD (grey value)	t	p	df	95 % CI		d	95 % CI	
							lower	upper		lower	upper
hyper-osmotic time segment	9	13419.87	2050.45	-6.63	0.000165	8	-1666	-806	0.60 (medium)	-0.42	1.63
iso-osmotic time segment	9	14655.78	2044.23								

b

Statistics of median RICM intensities over different curvature types.

	Statistics			One-way ANOVA					
Curvature type	N	Mean (grey value)	SD (grey value)		Sum sq.	df	Mean sq.	F	P
Flat	12	549.56	256.24	Between groups	394302	2	197151	3.73	0.034
Hill	12	412.25	211.47	Within groups	1903688	36	52880		
Valley	12	657.7	226.61						

Tukey HSD post hoc test					Cohen D		
Comparison	diff.	95 % CI		adj. P	d	95 % CI	
		lower	upper			lower	upper
Hill-Flat	-137.32	-353.81	79.18	0.280	-	-	-
Valley-Flat	108.14	-116.88	333.15	0.476	-	-	-
Hill-Valley	245.45	24.33	466.58	0.027	-1.12 (large)	-0.25	-2.00

Table S4.

Tables of statistical analysis of median RICM intensities subjected to osmolarity perturbations and over curvature types. a, Two-tailed paired student's t-test and effect size between the median RICM intensities over hyper- and iso-osmotic treatment timeframes. **b**, 1-way ANOVA of median RICM intensities over different curvature types, and Tukey HSD post hoc test statistics for the curvature type comparisons along with the effect size calculated for the significant pair (hill-valley).

a

Source of variation	Sum of squares	Degrees of freedom	Mean square	F	p-value
Permeability	0.585022	2	0.293	53.3434	2.330×10^{-14}
Within	0.350947	64			
Total	0.936	66			

b

Sample 1	Mean	Std	Sample 2	Mean	Std	Difference	DOF	Welch T stat	p-value	95% Cohen D
Polyacrylamide	0.105	0.078	Control	0.273	0.065973	-0.168	23.3	-6.316	1.815×10^{-6}	[-0.957, -3.143]
CY52	0.370	0.076	Control	0.273	0.065973	0.096	38.9	4.801	2.349×10^{-5}	[0.618, 1.850]

Table S5.

Tables of statistical analysis on varying the substrate permeability. **a**, 1-way ANOVA of varying the substrate on the normalized extrusion rates. **b**, Post hoc t-test statistics for the comparisons made.

a

Source of variation	Sum of squares	Degrees of freedom	Mean square	F	p-value
Intercept	1.901	1	1.901	291.835	6.522×10^{-43}
Curvature	0.160	2	0.080	12.265	5.664×10^{-1}
Treatment	0.507	2	0.254	38.944	2.612×10^{-15}
Interaction	0.303	4	0.076	11.636	1.253×10^{-8}
Within	1.511	232			
Total	4.383	241			

b

Simple effect	Source of variation	Sum of squares	Degrees of freedom	Mean square	F	p-value
Hill	Osmolarity	0.340	2	0.170	21.708	2.026×10^{-8}
	Within	0.705	90			
	Total	1.045	92			
Valley	Osmolarity	2.017	4	0.504	138.930	2.150×10^{-48}
	Within	0.523	144			
	Total	2.539	148			
Flat	Osmolarity	0.985	4	0.246	60.805	1.200×10^{-22}
	Within	0.300	74			
	Total	1.284	78			
FAKI14	Curvature	0.242	2	0.121	17.806	8.113×10^{-7}
	Within	0.414	61			
	Total	0.655	63			

c

Group	Sample 1	Mean	Std	Sample 2	Mean	Std	Difference	DOF	Welch T	Adj. p-value	95% Cohen D
Hill	FAKI14	0.217	0.051	Sucrose	0.134	0.067	0.083	54.9	5.335	3.724×10^{-6}	[0.896, 1.983]
				Control	0.267	0.120	-0.050	50.7	-2.227	3.040×10^{-2}	[-0.078, -0.973]
Valley	FAKI14	0.400	0.124	Sucrose	0.117	0.051	0.283	17.5	8.761	1.679×10^{-7}	[2.709, 4.795]
				Control	0.361	0.077	0.040	20.4	1.177	2.529×10^{-1}	-
Flat	FAKI14	0.280	0.073	Sucrose	0.115	0.065	0.165	43.0	7.970	1.051×10^{-9}	[1.718, 3.374]
				Control	0.273	0.066	0.006	38.6	0.292	7.715×10^{-1}	-
FAKI14	Valley	0.400	0.124	Hill	0.217	0.051	0.183	18.3	5.603	2.393×10^{-5}	[1.467, 3.190]

Table S6.

Tables of statistical analysis on the addition of FAKI14 inhibitor. a, 2-way ANOVA analysis to determine if addition of FAKI14 and curvature have an effect on the normalized extrusion rates. **b**, 1-way ANOVA of the simple effects on the normalized extrusion rates. **c**, Post hoc t-test statistics for the comparisons made with regard to the various experimental conditions.

Target	Host	Type	Dilution	Incubation Time (h)	Manufacturer	Cat. No.
AKT (pan)	Rabbit	Monoclonal	1:1000	24	CST	4691
Phospho-AKT (Ser473)	Rabbit	Monoclonal	1:1000	48	CST	4060
FAK	Mouse	Monoclonal	1:500	48	BD Biosciences	611008
Phospho-FAK (Try397)	Rabbit	Monoclonal	1:1000	48	Thermo Scientific	700255
GAPDH	Mouse	Monoclonal	1:1000	24	Santa-Cruz Biotech	32233

Table S7.

Dilution factors, incubation duration and manufacturer's catalogue numbers for immunoblotting.

Statistics of pFAK/FAK fluorescence intensity ratios over hills and valleys.

	Statisitics			Two-tailed student's t-test					Cohen D		
Curvature type	N	Mean (pFAK/FAK ratio)	SD (pFAK/FAK ratio)	t	P	df	95 % CI		d	95 % CI	
							lower	upper		lower	upper
Hill	9	0.882	0.039	8.330	3.269×10^{-7}	16	0.108	0.182	3.927 (large)	2.217	5.637
Valley	9	0.737	0.034								

Table S2.

Statistical analysis of p-FAK/FAK fluorescence intensity ratios over hills and valleys.

Movie S1.

24-hour time-lapse of confluent MDCK monolayers on wave substrates with 200 µm half-period dimension.

Movie S2.

24-hour time-lapse of confluent MDCK monolayers on wave substrates with 100 µm half-period dimension.

Movie S3.

24-hour time-lapse of confluent MDCK monolayers on wave substrates with 50 µm half-period dimension.

Movie S4.

Time-lapse showing convolution neural net cell extrusion event registration. Registered events marked out in false cyan.

Movie S5.

24-hour time-lapse of confluent MDCK monolayers on rectangular wave substrates with 200 µm half-period dimension.

Movie S6.

24-hour time-lapse of confluent MDCK monolayers on rectangular wave substrates with 100 µm half-period dimension.

Movie S7.

24-hour time-lapse of confluent MDCK monolayers on rectangular wave substrates with 50 µm half-period dimension.

Movie S8.

Time-lapse showing caspase 3/7 activation in monolayers on 100 µm wave substrates. Apoptotic cells are accompanied by fluorescence (false green).

Movie S9.

Valley-hill overlaid time-lapse showing the formation of fluid-filled domes (white arrows) on 100 µm wave substrates when imaged beyond 48 hours. The domes preferentially appear in valleys.

Movie S10.

24-hour time-lapse of confluent MDCK monolayers on 100 µm wave substrates subjected to hyper-osmotic media containing 4.1 wt. % sucrose.

Movie S11.

24-hour time-lapse of confluent MDCK monolayers on 100 µm wave substrates subjected to hyper-osmotic media containing 1 % DMSO.

Movie S12.

24-hour time-lapse of confluent MDCK monolayers on 100 μm wave substrates subjected to hyper-osmotic media containing 0.4 wt. % NaCl.

Movie S13.

24-hour time-lapse of confluent MDCK monolayers on 100 μm wave substrates subjected to hypo-osmotic media containing 25 % water.

Movie S14.

24-hour time-lapse of sub-confluent MDCK cells on 100 μm wave substrates subjected to hypo-osmotic media containing 25 % water.

Movie S15.

RICM time-lapse of MDCK monolayers on a planar surface. Dark streaks are locations of adhesions and brighter regions indicate fluids spaces. The time-lapse show numerous fluid spaces that is continuously in motion as indicated by the overlaid path-lines calculated from optical flow analysis.

Movie S16.

RICM time-lapse of MDCK monolayers on planar surface conditioned in hyper-osmotic media before iso-osmolarity is reinstated with the addition of water. The time-lapse demonstrate that monolayer basal fluids are responsive to osmotic perturbations. Several large fluid spaces can be seen towards the end.

Movie S17.

24-hour time-lapse of confluent MDCK monolayer on planar polyacrylamide hydrogel. These substrates buffer basal hydraulic stress and reduces cell extrusions.

Movie S18.

24-hour Time-lapse of confluent MDCK monolayers on 100 μm wave substrates subjected to hyper-osmotic media containing 4.1 wt. % sucrose and 3 μM FAK inhibitor 14.

Movie S19.

24-hour Time-lapse of confluent MDCK monolayers on 100 μm wave substrates subjected to hyper-osmotic media containing 4.1 wt. % sucrose and 6 μM FAK inhibitor 14.